ADVANCING EARTH AND SPACE SCIENCES

JGR Planets

RESEARCH ARTICLE
10.1029/2025JE009528

How Does Ice Shell Geometry Shape Ocean Dynamics on Icy Moons?

Yixiao Zhang[1], Wanying Kang[1], and John Marshall[1]

[1]Earth, Atmospheric, and Planetary Sciences, Massachusetts Institute of Technology, Cambridge, MA, USA

Key Points:
- Ice shell topography drives ocean circulation by inducing lateral temperature gradients through suppression of the freezing point of water
- The resulting thermal wind supports baroclinic eddies that are very efficient in meridional heat transport
- Sloped topography weakens or strengthens heat transport depending on salinity, which sets the sign of the thermal expansion coefficient

Correspondence to:
Y. Zhang and W. Kang,
yixiaoz@mit.edu;
wanying@mit.edu

Citation:
Zhang, Y., Kang, W., & Marshall, J. (2026). How does ice shell geometry shape ocean dynamics on icy moons? *Journal of Geophysical Research: Planets*, *131*, e2025JE009528. https://doi.org/10.1029/2025JE009528

Received 9 DEC 2025
Accepted 25 JUN 2026

Abstract A poleward-thinning ice shell can drive circulation in the subsurface oceans of icy moons by imposing a meridional temperature gradient–colder at the equator than the pole–through the freezing point suppression due to pressure. This temperature gradient sets a buoyancy gradient, whose sign depends on the thermal expansion coefficient determined by ocean salinity. Together with vertical mixing, this buoyancy forcing shapes key oceanic features, including zonal currents in thermal wind balance, baroclinic instability of those currents, meridional heat transport by eddies, and vertical stratification. We use high-resolution numerical simulations to explore how variations in ice shell thickness affect these processes. Our simulations span a wide range of topographic slopes, pole-to-equator temperature differences, and vertical mixing strengths, for both fresh and salty oceans. We find that baroclinic eddies dominate large-scale circulation and meridional heat transport, consistent with studies assuming a flat ice-ocean interface. However, sloped topography introduces new effects: when lighter water overlies denser water along the slope, circulation weakens as a stratified layer thickens beneath the poles. Conversely, when denser water lies beneath the poles, circulation strengthens as topography increases the available potential energy. We develop a scaling framework that predicts heat transport and stratification across all simulations. Applying this framework to Enceladus, Europa, and Titan, we infer ocean heat fluxes, stratification, and tidal energy dissipation, showing large-scale circulation constrains tidal heating and links future observations of ice thickness and rotation to subsurface ocean dynamics.

Plain Language Summary Icy moons such as Enceladus and Europa host oceans beneath thick ice shells that are typically thinner at the poles than at the equator, likely due to stronger tidal heating near the poles. This topography drives a meridional temperature gradient through pressure-dependent freezing point suppression, creating a buoyancy gradient that powers ocean circulation. The direction of this circulation depends on the thermal expansion coefficient of water, which changes sign between fresh and salty oceans near the freezing point. Using high-resolution numerical simulations, we investigate how variations in ice shell shape affect ocean stratification, zonal currents, and meridional heat transport. We find that baroclinic eddies–swirling motions arising from instabilities of zonal flows—dominate meridional heat transport. Sloped topography strongly modulates circulation: when denser water lies beneath the poles, circulation strengthens; when lighter water lies beneath the poles, it weakens. We develop scaling laws that predict ocean heat transport and stratification across a wide parameter range. Applying them to Enceladus, Europa, and Titan, we find that ocean circulation can limit the amount of tidal energy stored in the ocean. These results suggest that surface observations–such as ice thickness and nonsynchronous rotation–could reveal signatures of subsurface ocean dynamics, with implications for habitability.

1. Introduction

Icy moons with subsurface oceans are compelling targets for the search for life beyond Earth. These worlds, including Europa, Enceladus, and Titan, harbor vast liquid water oceans beneath their icy shells (Carr et al., 1998; Khurana et al., 1998; Kivelson et al., 2000; Pappalardo et al., 1999; Thomas et al., 2016), providing potentially habitable environments (Chyba, 2000; Glein & Waite, 2020; Russell et al., 2017; Taubner et al., 2018). Ocean circulation plays a key role in determining the habitability of icy moon oceans by transporting nutrients and chemical species and maintaining the chemical gradients that provide energy for life (Weber et al., 2023). It also controls transport time scales, determining whether chemical signatures and potential biosignatures can survive long enough to be transported to the surface for detection (Ames et al., 2025; Kang, Marshall, et al., 2022; Zeng & Jansen, 2021). Understanding the patterns of ocean circulation and the driving mechanisms in these bodies is crucial to assessing their habitability and interpreting observations of their surface features and potential biosignatures.

The poleward thinning of the ice shell, likely ubiquitous on icy moons due to the poleward amplified tidal heating pattern (Beuthe, 2018; Ojakangas & Stevenson, 1989), can drive ocean circulation by inducing under-ice temperature and consequent buoyancy gradients. As the thickness of the ice shell decreases poleward, the pressure at the ice-ocean interface drops, causing the freezing point to rise. This temperature increase makes the water there denser or lighter than in the equatorial region for positive and negative thermal expansion coefficients, respectively (further discussed in Section 2.1). The resulting buoyancy difference Δb, when transmitted into the interior by vertical mixing, can induce zonal currents which are prone to baroclinic instability. The resulting eddies transport heat down the gradient, from the polar regions to the equator (Zhang et al., 2024). This circulation and the resultant heat transport have been investigated by Zhu et al. (2017); Lobo et al. (2021); Kang (2022); Zhang et al. (2024) using idealized models, theoretical scaling laws, and numerical 3D simulations. The scaling law derived in Kang (2022) and Zhang et al. (2024) neglected the actual topography, the fact that the cold water under equatorial ice is lower in elevation than the warm water under the polar ice shell.

The difference in the elevations of buoyant and dense water sources strongly influences the overturning strength and the stratification of the ocean. From an energetic perspective, the relative height of the buoyancy source and sink determines whether the gravitational potential energy stored in the ocean will increase or decrease through buoyancy forcing (Jansen et al., 2023). Our goal here is to expand on our previous studies (Kang, 2022; Zhang et al., 2024), and to present a quantitative scaling law that accounts for the tilt of the ocean top and how it affects meridional heat transport and ocean stratification. Our scaling framework becomes a powerful tool for linking key components of the moon system—including ice geometry (Kang, 2022; Kang & Flierl, 2020; Kang & Jansen, 2022), mean ocean salinity (Kang, Mittal, et al., 2022; Zeng & Jansen, 2021), tidal dissipation, the ice shell's energy balance, and the moon's non-synchronous rotation (Ashkenazy et al., 2023; Kang, 2024)—through the lens of large-scale ocean circulation.

Our paper is set out as follows. Section 2 describes the setup of our numerical model and key physical parameters. Section 3 describes representative equilibrium solutions. Section 4 presents our scaling theory, including an analysis of the heat balance and energetics of the eddy field. Section 5 tests these scaling predictions against these equilibrium solutions. Section 6 explores how different parameters affect ocean circulation, and discusses the upper bound on the heat flux. Section 7 discusses the implications for icy moon oceans.

2. Model Setup

2.1. Under-Ice Buoyancy Forcing

Poleward-thinning ice shells create an equator-to-pole temperature difference under the ice, denoted ΔT, with warmer temperatures at the poles and cooler temperatures at the equator. The upper boundary of an icy moon's subsurface ocean is defined by the overlying ice, where the temperature equals the local freezing point, T_{freezing}. Because T_{freezing} depends on pressure, a lateral gradient in ice thickness ΔH_i induces a corresponding temperature gradient beneath the ice.

Assuming hydrostatic equilibrium, the induced temperature difference is:

$$\Delta T = \rho_w g \Delta H \frac{\mathrm{d}T_{\text{freezing}}}{\mathrm{d}p}, \tag{1}$$

where ρ_w is the density of water, g is the gravitational acceleration, and $\mathrm{d}T_{\text{freezing}}/\mathrm{d}p$ is the pressure sensitivity of the freezing point. This sensitivity (approximately $8 \times 10^{-8}\ \mathrm{K\,Pa^{-1}}$) depends only on the latent heat of melting and the density difference between water and ice, as constrained by the Clausius-Clapeyron relation. Here, ΔH is the elevation difference of the topography of the water-ice interface (Figure 1b). Assuming isostatic compensation (i.e., equal pressure at depth under hydrostatic balance) (Hemingway & Mittal, 2019; McKinnon & Schenk, 2021; Tajeddine et al., 2017; Čadek et al., 2016) and neglecting spatial variations in g within the ocean and ice shell, $\Delta H = (\rho_i/\rho_w)\Delta H_i$, where ρ_i is the density of ice. This relation follows from hydrostatic balance: a thickness variation ΔH_i in the ice shell produces a pressure anomaly $\rho_i g \Delta H_i$, which is balanced by a height variation ΔH in the ocean that produces $\rho_w g \Delta H$.

Due to the generally poleward-amplified tidal heating pattern, we focus on cases with poleward-thinning ice shells, resulting in $\Delta T > 0$–i.e., warmer poles and cooler equator (Figure 1a).

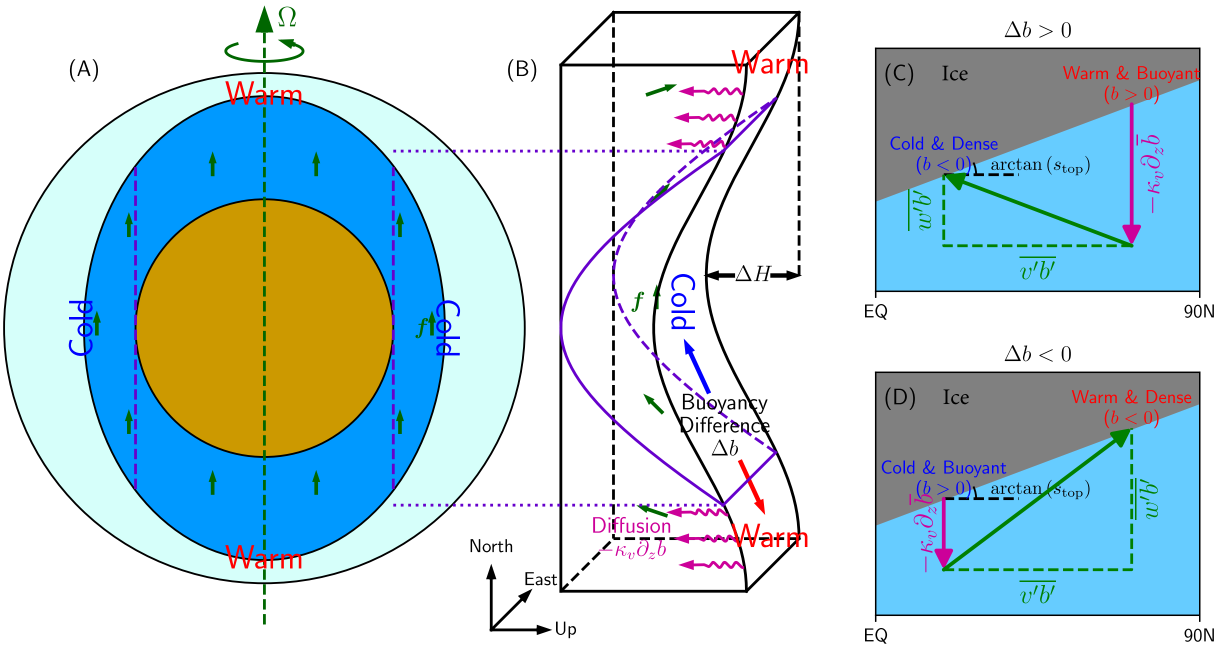

Figure 1. Setup of our numerical simulations and schematic for buoyancy transport beneath a tilted ocean-ice interface. Panel (a) illustrates an idealized icy moon with a poleward-thinning ice shell. This ice shell thickness gradient creates a meridional temperature gradient at the water-ice interface ("Cold" and "Warm" in Panel (a)) due to freezing point suppression by high pressure. The resulting temperature contrast ΔT leads to a buoyancy contrast $\Delta b = \alpha g \Delta T$, where α is the thermal expansion coefficient and g is the gravitational acceleration. The sign of Δb depends on the sign of α. This buoyancy gradient drives ocean circulation, which, under background rotation (indicated by arrows in Panel (a)), gives rise to baroclinic eddies—referred to as "ocean weather systems" in Zhang et al. (2024). Panel (b) depicts the numerical setup. Simulations are conducted in a Cartesian coordinate system. The poleward-thinning ice shell is represented as a tilted upper boundary with an elevation difference ΔH (see Equation 4). A buoyancy contrast, consistent with the imposed temperature difference, is prescribed as a boundary condition at the ocean top (Equation 6) and diffuses into the ocean interior via vertical diffusion ($-\kappa_v \partial_z b$ in Panel (b)). The Coriolis force is implemented in Cartesian coordinates by conserving the angle between the rotation vector **f** (green arrows in Panel (b)) and gravity, following Bire et al. (2022); Zhang et al. (2024). Parameters for each simulation are listed in Table 1. Panels (c, d) show schematics of buoyancy transport beneath a tilted ocean surface with constant slope s_{top} in the northern hemisphere. The pole-to-equator buoyancy difference Δb can be positive or negative depending on the sign of the thermal expansion coefficient α_T. The purple and green arrows represent vertical diffusion and eddy transport of buoyancy, respectively. At equilibrium, the vector sum of these two fluxes must be parallel to the tilted upper boundary, or otherwise the global-mean buoyancy of the ocean will evolve (Equation 12; derived and physically interpreted in Appendix A). The same quantities are shown in Figures 2 and 3, which resemble these schematics.

This temperature difference beneath the ice leads to a buoyancy difference, Δb, which can drive ocean circulation. We adopt an idealized equation of state with a constant thermal expansion coefficient α_T in each simulation and neglect the effects of salinity variations due to ice dynamics (Ashkenazy & Tziperman, 2021; Ashkenazy et al., 2018; Kang, Mittal, et al., 2022; Lobo et al., 2021; Zhu et al., 2017). The buoyancy, defined as $b = -g\,\delta\rho/\rho_w$, where $\delta\rho$ is the density anomaly, is linearly related to the temperature as:

$$b = \alpha_T g (T - T_0), \tag{2}$$

with T_0 as a reference temperature. The corresponding buoyancy difference is:

$$\Delta b = \alpha_T g \Delta T, \tag{3}$$

where α_T may be positive or negative depending on whether the ocean is sufficiently salty to offset the anomalous expansion of water (Bire et al., 2023; Kang, Mittal, et al., 2022; Zeng & Jansen, 2021). In this study, we explore both positive and negative Δb values (Table 1). Since ΔT is always positive (reflecting poleward-thinning ice), the sign of Δb is entirely determined by the sign of α_T.

2.2. Governing Equations and Model Details

We consider ocean circulation driven by the buoyancy gradient along the water-ice interface, induced by pressure-dependent freezing point suppression (Figure 1). The essential ingredients of this circulation include: (a)

Table 1
Simulation Parameters

Group	Simulation	Δb $(10^{-5}\ \mathrm{m\,s^{-2}})$	ΔH (km)	κ_v $(10^{-2}\ \mathrm{m^2\,s^{-1}})$
Control ($\Delta b > 0$)	ctrl$^+$ ◆	1.670	6	1.0
Varying Δb	b1$^+$ ★	*0.167*	6	1.0
	b2$^+$ ★	*0.501*	6	1.0
	b3$^+$ ★	*5.010*	6	1.0
	b4$^+$ ★	*16.700*	6	1.0
Varying ΔH	h1$^+$ ■	1.670	*0*	1.0
	h2$^+$ ■	1.670	*3*	1.0
	h3$^+$ ■	1.670	*12*	1.0
	h4$^+$ ■	1.670	*20*	1.0
Varying κ_v	k1$^+$ ▲	1.670	6	*0.1*
	k2$^+$ ▲	1.670	6	*0.3*
	k3$^+$ ▲	1.670	6	*3.0*
	k4$^+$ ▲	1.670	6	*10.0*
Control ($\Delta b < 0$)	ctrl$^-$ ◆	−1.670	6	1.0
Varying Δb	b1$^-$ ★	*−0.167*	6	1.0
	b2$^-$ ★	*−0.501*	6	1.0
	b3$^-$ ★	*−5.010*	6	1.0
	b4$^-$ ★	*−16.700*	6	1.0
Varying ΔH	h1$^-$ ■	−1.670	*0*	1.0
	h2$^-$ ■	−1.670	*3*	1.0
	h3$^-$ ■	−1.670	*12*	1.0
	h4$^-$ ■	−1.670	*20*	1.0
Varying κ_v	k1$^-$ ▲	−1.670	6	*0.1*
	k2$^-$ ▲	−1.670	6	*0.3*
	k3$^-$ ▲	−1.670	6	*3.0*
	k4$^-$ ▲	−1.670	6	*10.0*

Note. In the table Δb is the equator-to-pole buoyancy difference prescribed at the ocean-ice interface (positive means dense water at the equator); ΔH is the elevation difference of the ocean-ice interface from the equator to the pole; κ_v is the vertical diffusivity of buoyancy. Simulation tags follow the following convention: letters indicate the group, with "ctrl" for the control set, "b" for varying Δb, and "h" for varying ΔH. The trailing $+$ or $-$ denotes the sign of Δb: $+$ for dense water at the equator and $-$ for light water at the equator. A symbol for each simulation is shown next to its tag and will be used consistently in the figures. The marker shape indicates which parameter is varied, while progressively darker colors denote increasing parameter values. Parameters which differ from the control simulations (ctrl$^+$ and ctrl$^-$) are italicized for emphasis. A diagram of the model setup is presented in Figure 1b.

an equator-to-pole under-ice buoyancy difference Δb that drives the flow, (b) an elevation difference at the water-ice interface between the origins of dense and buoyant water masses, (c) vertical diffusion that transmits the upper-boundary buoyancy gradient into the ocean interior, and (d) the Coriolis force. As illustrated in Figure 1, the key physical parameters controlling the ocean dynamics include the equator-to-pole buoyancy contrast Δb, the ice thickness variation ΔH, the vertical diffusivity κ_v, and the moon's rotation rate Ω, its radius a, and mean ocean depth D.

To represent the system in numerical simulations, we follow a similar approach to (Zhang et al., 2024) but with a key modification: we account for the actual ice topography using immersed boundary conditions instead of a flat top boundary. We use a Cartesian coordinate system configured to represent flow in a spherical shell, as sketched in Figure 1b. The extent of the domain in the eastward x and northward y directions are $[0, L_x]$ and $[-(\pi/2)a, (\pi/2)a]$ respectively, where L_x is the zonal domain size, a is the planetary radius. The elevation of the ocean top is set to a cosine function:

$$z_{\text{top}} = -\frac{1}{2}\Delta H \cos(2y/a), \tag{4}$$

and the ocean bottom is always at $-D$. The western ($x = 0$) and eastern ($x = L_x$) boundaries are periodic.

Our governing equation is the rotating, non-hydrostatic equations for a Boussinesq fluid (referred to as the Boussinesq model):

$$\begin{cases} \partial_t \mathbf{u} + \mathbf{u}\cdot\nabla\mathbf{u} + \mathbf{f}\times\mathbf{u} = -\nabla P + b\mathbf{e}_z + \nu_h \nabla_h^2 \mathbf{u} + \nu_v \partial_z^2 \mathbf{u}; \\ \partial_t b + \mathbf{u}\cdot\nabla b = \kappa_h \nabla_h^2 b + \kappa_v \partial_z^2 b; \\ \nabla\cdot\mathbf{u} = 0, \end{cases} \tag{5}$$

where $\mathbf{u} = (u, v, w)$ is the vector form velocity; $\mathbf{f}$ is the Coriolis parameter (defined in Equation 7; green arrows in Figures 1a and 1b); P is the pressure divided by the reference density, a diagnostic field to keep $\mathbf{u}$ divergence-free; b is buoyancy; ν and κ represent viscosity and diffusivity, and the subscripts v and h represent the vertical and horizontal components, respectively. The Boussinesq model (Equation 5) uses buoyancy b instead of temperature T as the prognostic field. To retrieve the temperature field T, one needs to use the equation of state (Equation 2).

At the top of the ocean, the buoyancy b is set to a cosine profile:

$$b_{\text{top}} = -\frac{1}{2}\Delta b \cos(2y/a). \tag{6}$$

The sign of $\partial_y b_{\text{top}}$ in the Northern Hemisphere is the same as Δb. The bottom, north, and south boundaries have zero normal flux. A linear frictional stress of $(-\gamma u, \ -\gamma v)$ is applied to the velocity components u and v at the top and bottom boundaries. In this study, γ is set to a constant of 1×10^{-4} m s^{-1} (Jansen et al., 2023).

The Coriolis parameter is chosen to mimic that in a spherical shell and is given by:

$$\mathbf{f} = 2\Omega \exp\left(\frac{z}{a}\right)\left(\cos\left(\frac{y}{a}\right)\mathbf{j} + \sin\left(\frac{y}{a}\right)\mathbf{k}\right) \tag{7}$$

This form guarantees that the angle between $\mathbf{f}$ and the local gravity vector is as it is on a rotating sphere, and that $\mathbf{f}$ is non-divergent, ensuring the conservation of potential vorticity in adiabatic inviscid flow (Dellar, 2011; Grimshaw, 1975).

We run a set of simulations to test how circulation strength and ocean heat transport vary with Δb (the contrast of equator-to-pole buoyancy), ΔH (the difference of ice thickness from equator-to-pole) and κ_v (the vertical diffusivity). The parameter choices are summarized in Table 1. In all simulations, $D = 30$ kilometer; $a = 252.3$ kilometer; $L_x = 102$ kilometer; the horizontal grid size is $\Delta x = \Delta y = 1.2$ kilometer and the vertical grid size $\Delta z = 0.6$ kilometer; κ_h and ν_h are set to $(\Delta x/\Delta z)^2\kappa_h$ and $(\Delta x/\Delta z)^2\nu_h$ respectively. All simulations are run until equilibrium is established, and the last 10,000 rotation periods are used for diagnostic purposes.

The Boussinesq model (Equation 5) is integrated with Oceananigans.jl (Ramadhan et al., 2020; Silvestri et al., 2025), a high-performance ocean general circulation model coded in Julia. We use a staggered Arakawa C-grid (Arakawa & Lamb, 1977) and a third-order Runge-Kutta method for time integration (Le & Moin, 1991). The advection terms are calculated with a fifth-order WENO (weighted essentially non-oscillatory advection) scheme (Shu, 2009; Silvestri et al., 2024). The topography at the top is represented by an immersed boundary (Mittal & Iaccarino, 2005). A non-hydrostatic solver is used and we use the conjugate gradient method preconditioned by a three-dimensional Fast Fourier Transform to calculate P in Equation 5.

3. Phenomenology of Ocean Circulation

In this section, we describe the ocean circulation and associated transport characteristics from simulations "h4$^+$" and "h4$^-$" (see Table 1 for the parameters of this simulation), which use positive and negative Δb, respectively,

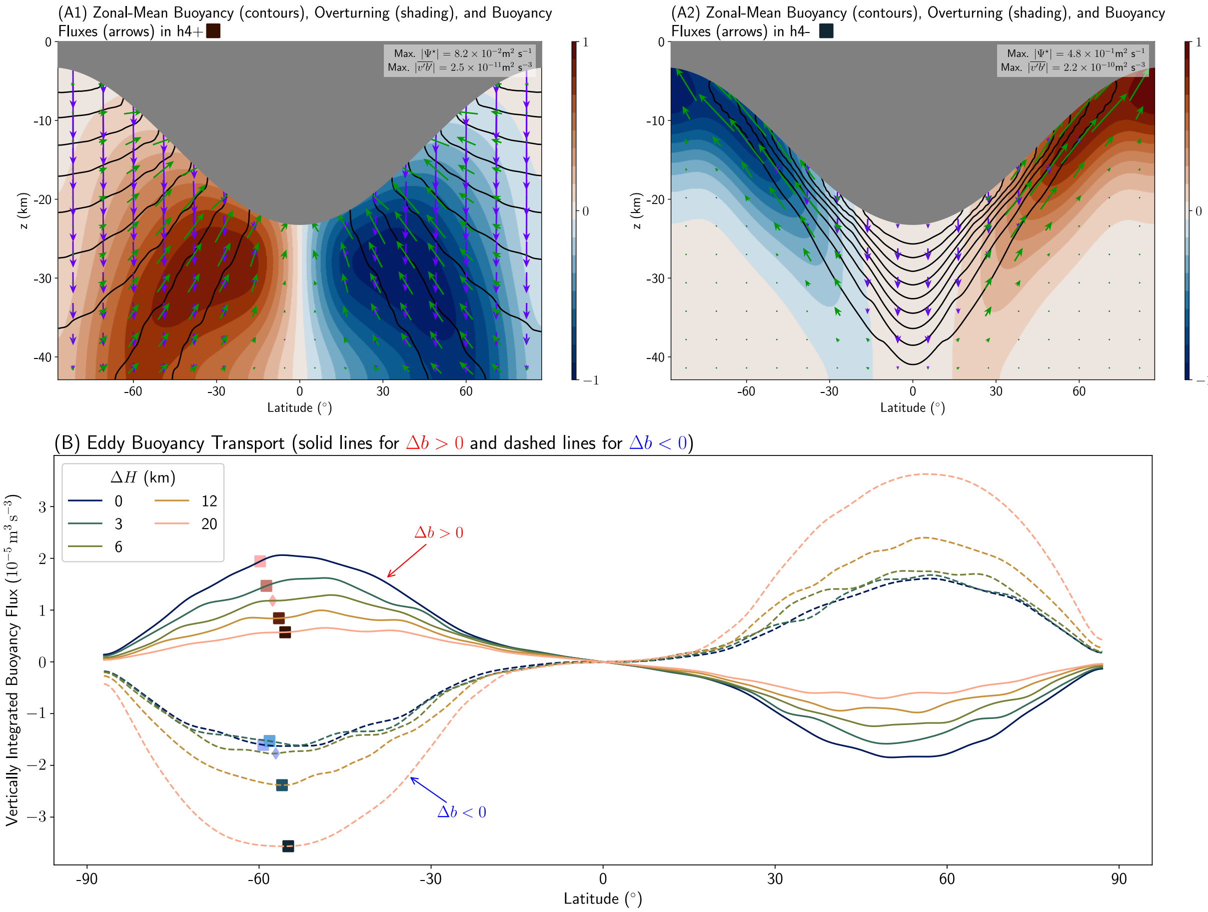

Figure 2. Ocean circulation and buoyancy transport in simulations h4$^+$ and h4$^-$ (see Table 1 for parameters). Panel (a1) corresponds to h4$^+$; Panel (a2) to h4$^-$. In Panels (a1 and a2), solid contours show buoyancy (contour interval = $|\Delta b|/10$), with buoyant water overlying denser water. Green and purple arrows denote eddy buoyancy flux $\left(\overline{v'b'}, \overline{w'b'}\right)$ and diffusive flux $\left(-\kappa_h \partial_y \overline{b},\ -\kappa_v \partial_z \overline{b}\right)$, normalized by the maximum $\overline{v'b'}$ (listed top right). The equivalent overturning circulation, diagnosed from Equation 9, is shown by $\psi^\star$ shading (normalized by its maximum; values listed). Negative $\psi^\star$ (blue) indicates counterclockwise overturning; positive (red) indicates clockwise overturning. Panel (b) shows vertically integrated buoyancy transport: solid lines for h1$^+$–h4$^+$ and ctrl$^+$ (varying ΔH; legend), dashed lines for h1$^-$–h4$^-$ and ctrl$^-$.

and both feature the largest topographic height difference ΔH. This case exemplifies the mechanisms that govern ocean circulation in all simulations in our study. These mechanisms are consistent with previous work prescribing lateral buoyancy gradients over flat boundaries (Kang, Mittal, et al., 2022; Zhang et al., 2024), although tilted topography can significantly influence circulation strength. This motivates the scaling framework developed in Section 4.

The flow is dominated by baroclinic eddies (Figures 2a1, 2a2). Eddies extract available potential energy from the large-scale meridional buoyancy gradient through baroclinic instability. Zonal jets also emerge as eddy kinetic energy is arrested at the Rhines scale by the β-effect (Rhines, 1975, 1979), consistent with prior findings (Bire et al., 2022; Heimpel & Aurnou, 2007; Zhang et al., 2024). These eddies generate buoyancy fluctuations that drive a down-gradient meridional buoyancy flux $v'b'$ which converges toward the equator for $\Delta b > 0$ and toward the poles for $\Delta b < 0$ (Figure 2).

The transport characteristics of ocean circulation, which is the focus of this study, can be described by an eddy-driven overturning. Similarly to Kang, Mittal, et al. (2022); Zhang et al. (2024), eddies dominate meridional heat transport, while the Eulerian mean flow contributes negligibly. Since turbulent flow is nearly adiabatic, the buoyancy flux (green arrows) aligns with isopycnals (contours) (Figure 2b):

$$\frac{\overline{w'b'}}{\overline{v'b'}} = -\frac{\partial_y \bar{b}}{\partial_z \bar{b}}. \tag{8}$$

This supports using a residual-mean streamfunction $\psi^\star$ to describe eddy transport (Plumb & Ferrari, 2005; Zhang et al., 2024):

$$\psi^\star = -\frac{\overline{w'b'}}{\partial_y \bar{b}}, \tag{9}$$

which is equivalently expressed as $\psi^\star = \overline{v'b'}/\partial_z \bar{b}$ (using Equation 8). In practice, we use Equation 9 because it remains well-defined throughout the domain. For $\Delta b > 0$, the overturning sinks at equator, the source of cold water, resulting in a counter-clockwise overturning (positive $\psi^\star$) in the Southern Hemisphere; for $\Delta b < 0$, the overturning sinks at the poles instead, reversing the direction of the overturning. We will see in Section 4.2 that the strength of overturning depends on the buoyancy gradient that energizes eddies and the background rotation of the moon, and a scaling for $\psi^\star$ will be given.

Vertical diffusion is essential to maintain the circulation. Unlike the Earth's ocean, where wind-driven Ekman pumping transfers surface buoyancy gradients downward, icy moon oceans lack such forcing. Instead, vertical diffusion must transport the buoyancy gradient from the ice-ocean interface to the interior. Energetically, a positive (upward) $\overline{w'b'}$ is required to maintain the eddy field, which must be balanced by a downward diffusive buoyancy flux–precisely what we observe in simulations (Figures 2a and 3).

For positive Δb (as in the case of "h4$^+$"), the sloped topography creates a thicker stratified layer below the poles (Figure 2a1). In this case, buoyant water sits higher at the poles than denser water at the equator, weakening circulation: vertical diffusion must penetrate deeper to transport buoyancy into the interior and trigger baroclinic instability. The decreasing meridional buoyancy transport with increasing ΔH (Figure 2b) supports this interpretation. This idea becomes further developed in Section 4.1 where a formula for the penetration depth is presented which depends on the strength of vertical diffusion (represented by κ_v) and the eddy overturning streamfunction (represented by the maximum of $|\psi^\star|$), following Kang, Mittal, et al. (2022); Zhang et al. (2024).

For negative Δb (as in the case of "h4$^-$"), the sloped topography provides a new pathway to energize the eddies. In this case, buoyant water at the equator can move upward along the tilted ocean top toward the poles. The upward eddy buoyancy $\overline{w'b'}$, which must be balanced by downward vertical diffusion in the previous case, can now be balanced by an exchange of buoyancy with the tilted upper boundary layer. As a result, the meridional buoyancy flux strengthens with increasing ΔH (Figure 2b). In addition, the depth of the stratified layer shrinks, leaving the major part of the ocean cold and almost free of baroclinic eddies. Comparing our simulation "h4$^+$" ($\Delta b > 0$) and "h4$^-$" ($\Delta b < 0$), the former has stratified layer (isopycnals shown by contours) and overturning circulation (meridional streamfunction shown by shading Figure 2a1)) extending from the ocean top almost to the bottom, but in the latter, both the stratified layer and overturning circulation are shallow (Figure 2a2).

Figure 3 shows how the equilibrium solutions change as the mixing (rows A and D), buoyancy parameters (rows B and E), and topography (rows C and F) are varied relative to the control. Their effects on the equilibrium flow are discussed in Section 5, after establishing the scaling relations in Section 4.

4. Scaling Theory

In this section, we derive the scaling laws that govern how (a) the meridional buoyancy (heat) flux by baroclinic eddies F_h and (b) the equilibrium buoyancy (temperature) distribution vary with planetary parameters and ocean diffusivity. To achieve this goal, we need to take two steps. First (in Section 4.1), we determine the equilibrium buoyancy distribution, characterized by the isopycnal slope s, since downward buoyancy diffusion balances upward buoyancy transport by eddies. Second (in Section 4.2), we determine the transport efficiency of baroclinic eddies, characterized by the residual overturning streamfunction $\psi^\star$, for a given isopycnal distribution s.

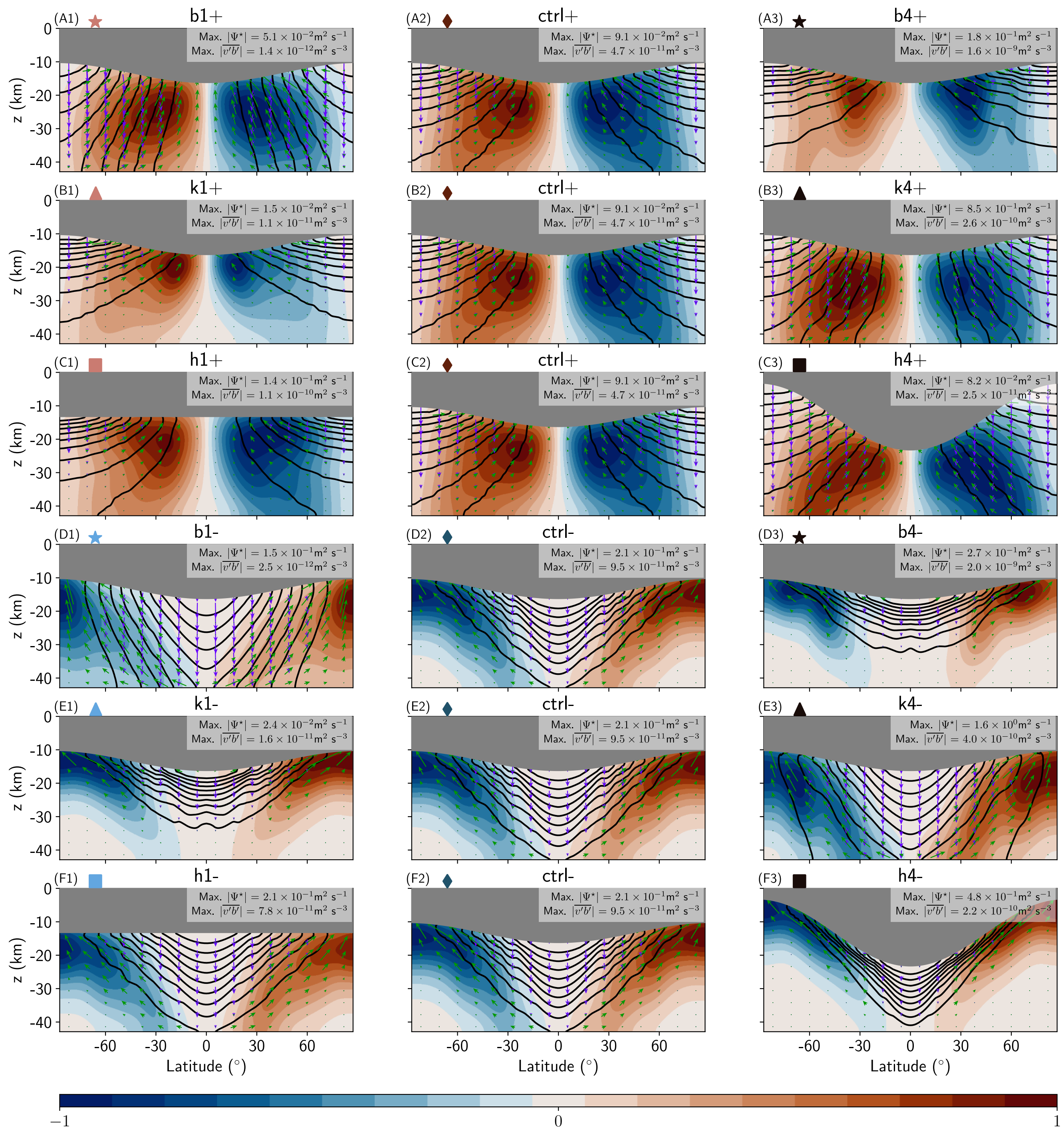

Figure 3. Zonal-mean buoyancy and buoyancy flux patterns from our numerical simulations. Each panel corresponds to one simulation (see Table 1 for parameters) and shows the same variables as Figure 2a The middle column shows the control experiment for $\Delta b > 0$ (top 3 panels) and $\Delta b < 0$ (bottom 3 panels). For convenience the panels presenting the control are repeated to ease comparison as parameters are changed moving left and right.

We focus on the regime in which isopycnals do not intersect the ocean bottom, similar to Lobo et al. (2021); Zhang et al. (2024). This regime is likely more representative of the realistic ocean of Enceladus because of its small vertical diffusivity. (Kang, 2022) examined both regimes and showed that when isopycnals reach the ocean floor, the scaling of the eddy-driven overturning changes slightly because the supercriticality ξ exceeds unity.

4.1. Buoyancy Distribution—The Competition Between Diffusion and Baroclinic Eddies

Here, we try to determine the equilibrium buoyancy distribution assuming that we know the circulation strength. For simplicity, this buoyancy distribution is characterized by one parameter, the isopycnal slope $s \equiv |\partial_y \overline{b}/\partial_z \overline{b}|$. Following Lobo et al. (2021); Kang and Jansen (2022); Zhang et al. (2024), s in the equilibrium state is determined by two competing effects. On the one hand, vertical diffusion, controlled by vertical diffusivity κ_v, brings the buoyancy gradient into the interior of the ocean, steepening the isopycnal and increasing the available potential energy of the ocean (Jansen et al., 2023). On the other hand, baroclinic eddies tap into this energy source and tend to flatten out the isopycnals (Ito & Marshall, 2008; Marshall & Radko, 2003). Since the turbulent mixing process is close to adiabatic, the eddy-induced heat transport should be directed along the isopycnals, and so the transport can be equivalently represented by an overturning circulation $\psi^\star$:

$$\overline{v'b'} \sim -\mathrm{sgn}(\Delta b)|\psi^\star|\partial_z \overline{b} \tag{10}$$

$$\overline{w'b'} \sim |\psi^\star||\partial_y \overline{b}| \tag{11}$$

where $\mathrm{sgn}(\Delta b)$ represents the sign of the equator-pole buoyancy gradient. A positive Δb corresponds to having denser water near the equator and vise versa. Note that the sign of $\overline{v'b'}$ and all variables in Section 4.1 is given for the northern hemisphere.

The total heat flux in the direction perpendicular to the top topography must vanish at equilibrium (see Appendix A for a more detailed explanation). In other words, $\left(\overline{v'b'}, \overline{w'b'}\right)$ is parallel to the top topography:

$$\underbrace{|\psi^\star||\partial_y \overline{b}|}_{\overline{w'b'}} - \kappa_v \partial_z b \sim s_{\mathrm{top}} \underbrace{\left(-\mathrm{sgn}(\Delta b)|\psi^\star|\partial_z \overline{b}\right)}_{\overline{v'b'}} \tag{12}$$

where s_{top} is the slope of the top topography. Dividing both sides of Equation 12 by $\overline{w'b'}$ and using $s = |\partial_y \overline{b}|/\partial_z \overline{b}$, we get a formula for the isopycnal slope s:

$$s + s_{\mathrm{top}} \mathrm{sgn}(\Delta b) \sim \kappa_v/|\psi^\star| \tag{13}$$

This tells us that when diffusion dominates ($\kappa_v > \psi^\star$), the isopycnal slope s would steepen and vice versa, consistent with the physical intuition presented at the beginning of this section. Furthermore, the topography slope s_{top} decreases s when they tilt in the opposite direction when $\Delta b > 0$ and increases s when $\Delta b < 0$. Appendix A presents a rigorous derivation of Equation 13 using the integral form of the heat flux balance.

We test Equation 13 against our simulations (Figure 4a). To measure s, we measure the slope of the median isopycnal s_{m}, by tracking its latitudinal and depth extent. To measure the amplitude of the eddy driven-overturning $\psi^\star_m$, we project the vertical heat flux $\overline{w'b'}$ onto the meridional buoyancy gradient $\partial_y \overline{b}$:

$$\psi^\star_{\mathrm{m}} = \frac{\int_{\mathcal{D}} |\overline{w'b'}\partial_y \overline{b}| \mathrm{d}y\, \mathrm{d}z}{\int_{\mathcal{D}} \left(\partial_y \overline{b}\right)^2 \mathrm{d}y\, \mathrm{d}z} \tag{14}$$

where $\mathcal{D}$ represents the ocean domain of (y, z). This form is similar to how we diagnose the spatial distribution of $\psi^\star$ (Equation 9). Here, we use an average over the domain to get the overall overturning strength. The topographic slope $s_{\mathrm{top}} \equiv \Delta H/((\pi/2)a)$. In Figure 4a, we show that the right-hand side and the left-hand side of Equation 13 scale with each other, suggesting that this formula captures how diffusion and baroclinic eddies jointly affect the slope of isopycnals. The fitted ratio $c_s = 1.38$ of the proportional relationship (Figure 4a) may be a result of our choice of how to diagnose $\psi^\star_m$ and s_m. We include the factor of c_s in our scaling framework for consistency.

4.2. Efficiency of Baroclinic Eddy Transport $\psi^\star$

In this section, we present a scaling law for the eddy-driven overturning $\psi^\star$ given an isopycnal slope.

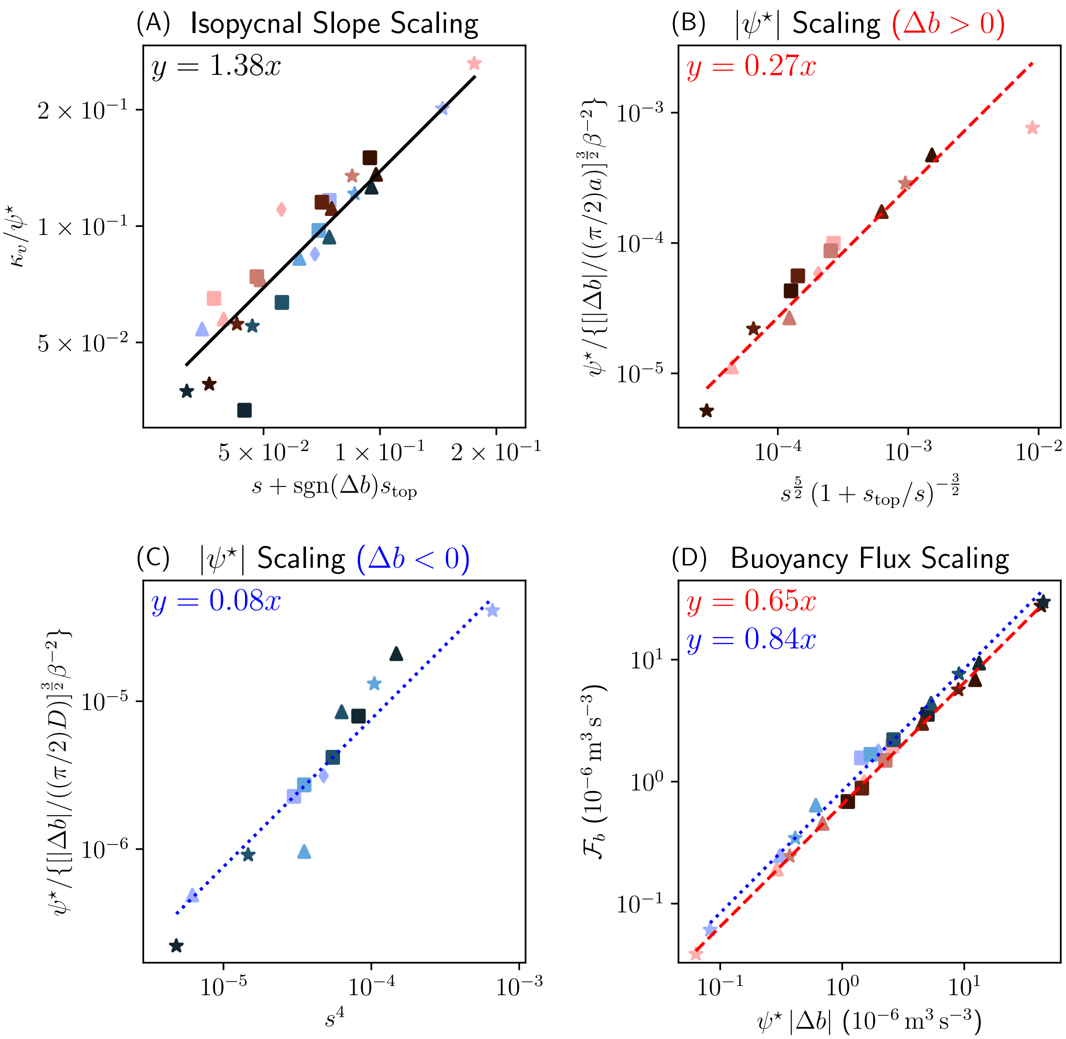

Figure 4. Tests of scaling theory against numerical simulations. Panel (a) shows a scaling for the isopycnal slope (Equation 13). Panel (b) and Panel (c) show the scaling for the eddy-driven overturning $\psi^\star$ for positive and negative Δb, respectively (Equation 24). Panel (d) shows the scaling for the vertical integrated meridional buoyancy flux (proportional to heat flux). Here, s represents the slope of the median isopycnal, s_m; $s_{\mathrm{top}} \equiv \Delta H/((\pi/2)a)$ is the slope of the top topography; $\psi^\star$ represents the mean overturning diagnosed using Equation 9; sgn(Δb) is the sign of the prescribed equator-to-pole buoyancy difference Δb; $\mathcal{F}_b$ is the maximum of the vertical integrated meridional buoyancy flux. In Panel (b, c), $\psi^\star$ is normalized using the buoyancy difference Δb, the moon radius a, the mean ocean depth D, and the β factor ($\beta \equiv 2\Omega/a$). The line and the formula at the upper left corner of each panel shows the best fit; the red dashed line and blue dotted lines represent the fit for positive and negative Δ cases, respectively. The marker and color of each simulation is the same as Figure 3. The parameters used in these simulations are set out in Table 1.

Following the Gent-McWilliams closure (Gent & Mcwilliams, 1990), the overturning streamfunction can be written as the product of the eddy diffusivity κ_e and the isopycnal slope s,

$$|\psi^\star| = \kappa_e s. \tag{15}$$

We can verify $|\overline{v'b'}| \sim \kappa_e|\partial_y \overline{b}|$ from Equation 10 as a way to motivate Equation 15.

To obtain scaling laws for $\psi^\star$, we first need to know how κ_e depends on the buoyancy profile b. Following the mixing-length theory, κ_e can be expressed as the product of the characteristic length scale of eddies L_e and their characteristic velocity V_e.

$$\kappa_e = kL_eV_e \tag{16}$$

where $k \sim 0.25$ is a constant.

To estimate the eddy length scale L_e and the velocity scale V_e, we follow the pioneering work of Held and Larichev (1996) and Gallet and Ferrari (2021). The physical picture presented in these works is as follows. On a β-plane, baroclinic eddies, once generated, cascade to increasingly larger scales until reaching the zonal scale L_β. Beyond L_β, most of the kinetic energy of the eddy is in the form of zonal jets, which do not transport buoyancy (heat) meridionally. Therefore, the characteristic size of the eddy L_e should scale with L_β:

$$L_e \sim L_\beta = \sqrt{V_e/\beta}. \tag{17}$$

At equilibrium, the rate at which baroclinic energy is generated $\dot{E}_{\text{bci}}$ should be equal to $\dot{E}_{L_\beta}$, the rate of energy transfer across L_β. The latter can be expressed as a function of the characteristic velocity V_e and characteristic length L_β (Galperin et al., 2008):

$$\dot{E}_{L_\beta} = V_e^3/L_\beta, \tag{18}$$

By equating $\dot{E}_{\text{bci}}$ and $\dot{E}_{L_\beta}$, Held and Larichev (1996) arrived at scaling laws for L_e and V_e.

To evaluate $\dot{E}_{\text{bci}}$, Held and Larichev (1996) and Gallet and Ferrari (2021) considered a two-layer quasi-geostrophic (QG) system. Although similar analyzes are possible for a tilted boundary (Mechoso, 1980), here we consider the energy release by baroclinic eddies in a 3D system:

$$\dot{E}_{\text{bci}} = \overline{w'b'} = s|\overline{v'b'}| = sV_eL_e|\overline{\partial_y b}|, \tag{19}$$

where $\overline{\partial_y b}$ denotes the meridional buoyancy gradient averaged from the surface, where the buoyancy gradient (and hence available potential energy, APE) is strongest, to the level where baroclinic instability actually occurs.

Setting Equation 18 and Equation 19 equal to each other yields

$$V_e = s|\overline{\partial_y b}|\beta^{-1},\ L_e \sim L_\beta = \left(s|\overline{\partial_y b}|\right)^{1/2}\beta^{-1}, \tag{20}$$

which, when combined with Equation 16, leads to

$$\kappa_e \sim \left(s|\overline{\partial_y b}|\right)^{\frac{3}{2}}\beta^{-2}. \tag{21}$$

This scaling shows how the meridional buoyancy gradient and the isopycnal slope affect the eddy transport efficiency.

To calculate $|\partial_y b|$, the meridional buoyancy gradient must be averaged over the region where baroclinic instability occurs and develops, which corresponds roughly to the vertical extent of the fastest-growing mode. When $\Delta b > 0$, polar fluid is denser than equatorial fluid, the potential vorticity (PV) gradient near the upper surface is of the opposite sign to that in the interior (dominated by the planetary β), satisfying the Charney-Stern criterion for instability (Charney & Stern, 1962). Since the upper surface is also where APE is concentrated, APE release does not depend on conditions at the bottom of the ocean, where buoyancy is constant. This suggests that $\overline{\partial_y b}$ should be averaged over the upper layer, where surface buoyancy anomalies penetrate, giving the result that

$$\overline{|\partial_y b|} \sim \frac{|\Delta b|}{(\pi/2)a}\frac{1}{1+s_{\text{top}}/s} \quad \text{for} \quad \Delta b > 0. \tag{22}$$

In contrast, when $\Delta b < 0$, the PV gradient near the bottom boundary surface is of opposite sign to the interior, so the Charney-Stern instability criterion is only satisfied in the lower part of the ocean. Since there is very little APE in the bottom ocean, only modes that extend the entire ocean depth can tap into the APE source. This justifies averaging $\partial_y b$ across the entire ocean is:

$$\overline{|\partial_y b|} \sim \frac{|\Delta b|}{(\pi/2)a}\frac{a\,s}{D} \tag{23}$$

where $a\,s$ is the ocean stratified layer depth.

Substituting Equations 22 or 23 into Equations 21 and 15, we get

$$|\psi^\star| = \begin{cases} c_\psi^+\left(\frac{|\Delta b|}{(\pi/2)a}\right)^{\frac{3}{2}}\beta^{-2}s^{\frac{5}{2}}(1+s_{\text{top}}/s)^{-\frac{3}{2}} & \text{for } \Delta b > 0; \\ c_\psi^-\left(\frac{|\Delta b|}{(\pi/2)a}\right)^{\frac{3}{2}}\beta^{-2}s^4(a/D)^{\frac{3}{2}} & \text{for } \Delta b < 0, \end{cases} \tag{24}$$

where c_ψ^+ and c_ψ^- are constants that can be obtained by regression analysis.

We test Equation 24 against our simulations (Figures 4b and 4c). The measured isopycnal slope and overturning stream function use the same definitions as Section 4.1. Although $\beta = (2\Omega/a)\sin\theta$ varies with latitude θ, for simplicity, we set β at $2\Omega/a$ when performing the scaling analysis, absorbing the influence of latitudinal dependence into c_ψ^+ or c_ψ^- in Equation 24. Panels (B) and (C) show a good agreement between simulations and our scaling, yielding $c_\psi^+ = 0.27$ and $c_\psi^- = 0.08$. However, we notice that individual simulation results may deviate slightly from the predicted trends due to intrinsic variability in turbulent flows, finite numerical resolution, and additional complexities that are not captured by the scaling, such as spatial variations in isopycnal slopes. These factors may explain the slight deviations of some simulation results from the predicted scaling. Overall, we have less confidence in the scaling for the case where $\Delta b < 0$ because of the possible onset of slantwise convection (Zeng & Jansen, 2026), although the simulations generally remain consistent with the scaling.

4.3. Prediction of Ocean Heat Transport

Combining Equations 13 and 24, one can solve for the isopycnal slope s. The combined equation is:

$$s^4(s+s_{\text{top}})^{-\frac{1}{2}} = \left(c_s c_\psi^+\right)^{-1}\kappa_v\left(\frac{|\Delta b|}{(\pi/2)a}\right)^{-\frac{3}{2}}\beta^2 \qquad \text{for} \quad \Delta b > 0; \tag{25}$$

$$(s-s_{\text{top}})\,s^4(as/D)^{\frac{3}{2}} = \left(c_s c_\psi^-\right)^{-1}\kappa_v\left(\frac{|\Delta b|}{(\pi/2)a}\right)^{-\frac{3}{2}}\beta^2 \qquad \text{for} \quad \Delta b < 0. \tag{26}$$

One can verify that the left hand side monotonously increases with s. For $\Delta b < 0$, s must be greater than s_{top} for the left hand side to be valid.

Once $|\psi^\star|$ is known, the implied meridional buoyancy transport $\mathcal{F}_b$ may be estimated by the following:

$$\mathcal{F}_b = c_F|\psi^\star||\Delta b|. \tag{27}$$

To measure $\mathcal{F}_b$ in a particular simulation, we first calculate the vertically integrated buoyancy flux as a function of y and then take the maximum as the characteristic value that we present in Figures 4d and 45. Here, c_F can be different for positive and negative Δb because the sign of Δb affects the direction in which the isopycnals tilt and therefore determines whether the stratification is centered at low or high latitudes. We fit these two cases separately and find good agreement between $\mathcal{F}_b$ and $|\psi_m^\star|\Delta b$ (Figure 4d). The fitted parameters are $c_F^+ = 0.65$ and $c_F^- = 0.84$ for positive and negative Δb, respectively.

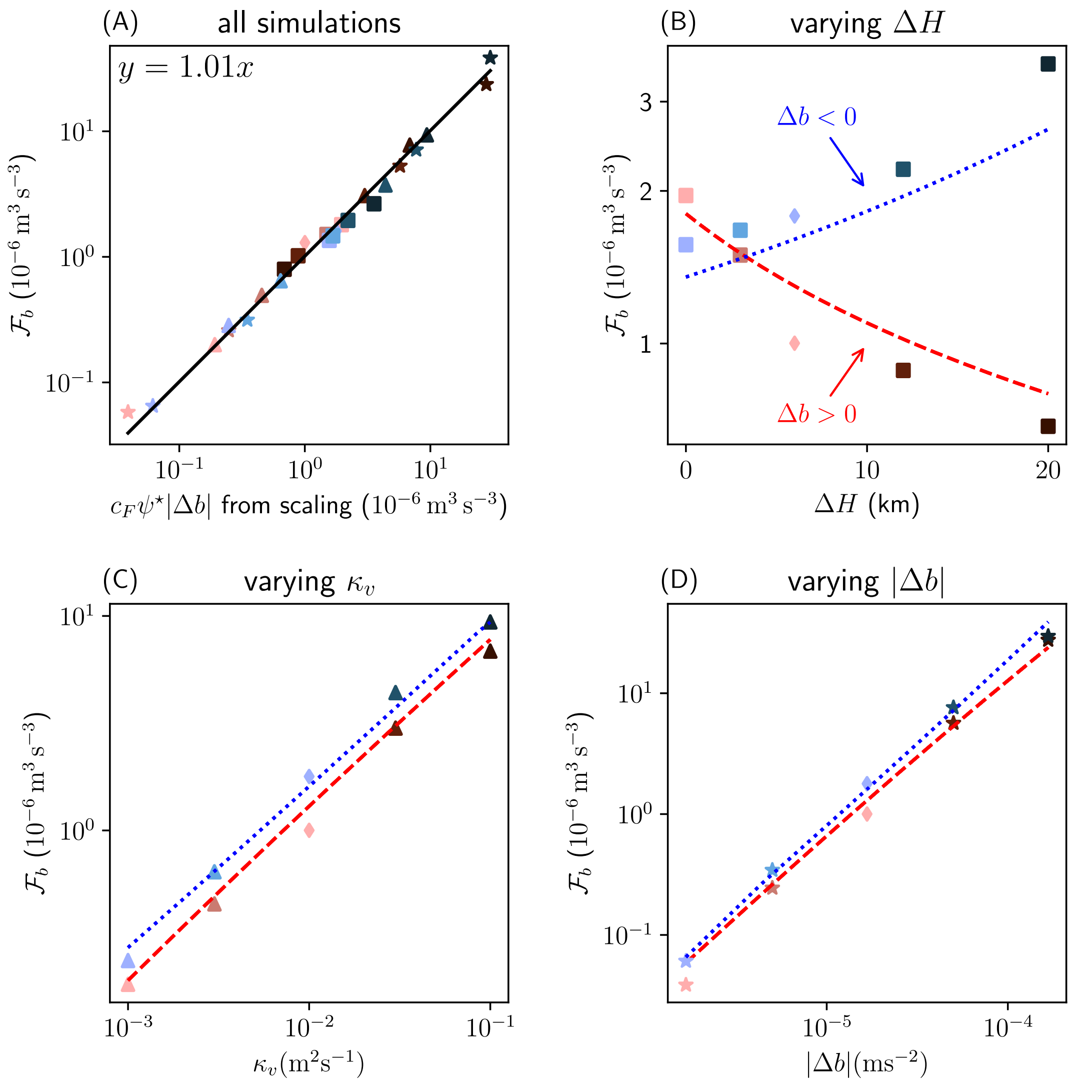

Figure 5. Meridional buoyancy fluxes in our simulations compared against predictions from our scaling framework. Our scaling framework first solves for s using Equation 25 when $\Delta b > 0$ and Equation 26 when $\Delta b < 0$. It then predicts the eddy-driven overturning strength $|\psi^\star|$ using Equation 24 and the meridional buoyancy transport $\mathcal{F}_b$ using Equation 27. Panel (a) plots the predicted vertically integrated meridional buoyancy transport $\mathcal{F}_b$ against the measured value (defined as the maximum along all latitudes) from each of our simulations. The solid line and the formula on the left upper corner show the best fit, and is almost the 1:1 line. Panels (b–d) show how ΔH, κ_v, and $|\Delta b|$ influences $\mathcal{F}_b$: the red dashed and blue dotted lines represent the predictions of our scalings for positive and negative Δb, respectively. All panels use a logarithmic y-axis scale. The parameters used in these simulations are tabulated in Table 1.

5. Effects of Key Parameters

We test our scaling for the vertically integrated meridional buoyancy flux, $\mathcal{F}_b$, using 26 numerical simulations spanning a range of ΔH, κ_v, and Δb (Figure 5). All data points fall along the 1:1 line, indicating general good agreement between simulations and scaling prediction (Figure 5a).

To understand how each individual parameter (ΔH, κ_v, and Δb) influences the buoyancy transport $\mathcal{F}_b$ and the underlying physical mechanisms, we revisit the conceptual framework. In our model setup (Figure 1), buoyancy varies along the upper surface, but unless this variation induces a non-zero meridional buoyancy gradient, there is no available potential energy to drive a circulation. When the water-ice interface is flat, as assumed in previous studies (Kang & Jansen, 2022; Zhang et al., 2024), vertical diffusion is essential to initiate baroclinic instability and allow heat transport. In this regime, the meridional buoyancy flux $\mathcal{F}_b$ scales as $\kappa_v^{5/7}$. This prediction can be derived by solving Equations 24, 25 and 27, and the resulting $5/7$ power law is confirmed by our numerical simulations (Figure 5c).

When topography is introduced, the above physical picture may be subject to changes. If denser fluid lies beneath thicker ice ($\Delta b > 0$), the stratification (measured by $\partial_z \overline{b}$) beneath thin ice is weakened due to the increased distance from the water-ice interface to a specific isopycnal. This reduced stratification weakens the vertical diffusive flux and thereby the meridional buoyancy transport, since the vertical and meridional buoyancy fluxes must balance in equilibrium (Equation 12). This trend is evident in our numerical simulations, as shown in Figures 3c and 5b.

In contrast, when the denser fluid lies beneath thinner ice ($\Delta b < 0$), the isopycnals bend toward the equator and are compressed by the protruding ice, enhancing vertical diffusion and meridional heat transport (Figure 3f). In this configuration, unlike the case with $\Delta b > 0$, the dynamics is not solely energized by downward diffusion. Instead, surface buoyancy forcing injects available potential energy into the system by densifying the ocean from above (Jansen et al., 2023). As a result, even in the limit $\kappa_v \to 0$, the meridional buoyancy transport does not vanish. This behavior is captured in Equation 24: substituting $s = s_{\mathrm{top}} > 0$ yields a non-zero $\psi^{\star}$. The dependence of $\mathcal{F}_b$ on ΔH in the case of negative Δb is shown in Figure 5b (blue line), which is in good agreement with the simulation results (blue markers).

Increasing the equator-to-pole buoyancy contrast $|\Delta b|$ initially strengthens the overturning circulation, lifting isopycnals upward (Figures 3a and 3d). According to the vertical buoyancy flux balance (Equation 12), this intensifies the vertical diffusive flux and, consequently, the meridional heat transport. After some mathematical manipulation, one can show that $\mathcal{F}_b \sim |\Delta b|^{10/7}$, consistent with the scaling laws derived in Kang and Jansen (2022); Zhang et al. (2024). This dependence is also consistent with our simulations (Figure 5d).

Δb is a prescribed constant in our simulations, but on realistic icy moons it is correlated with many other parameters, including ΔH, α, and g (which increases with the moon radius a). We apply our scaling to realistic icy moons, including Enceladus, Europa, and Titan, to predict the ocean heat transport there in Section 7.

6. Implication for Icy Moons

6.1. Role of Topography on Realistic Icy Moons

A key question is to what extent topography influences ocean circulation on realistic icy moons. To investigate this, we focus on the thickness of the stratified layer, d, defined as the maximum vertical distance between the median isopycnal and the ocean surface. This thickness can be expressed as $(\pi/2)a(s_m + s_{\mathrm{top}}\mathrm{sgn}(\Delta b))$, where s_m is the slope of the median isopycnal (introduced in Section 4 and shown in Figure 4) and s_{top} is the slope at the top of the ocean.

We examine how the stratified layer thickness d depends on ΔH, the topographic height difference, and on $d^{(\mathrm{flat})}$, the stratified layer thickness for a flat ocean top. The latter has been extensively studied by Kang, Mittal, et al. (2022) and Zhang et al. (2024). Figure 6 shows $d/d^{(\mathrm{flat})}$ plotted against $\Delta H/d^{(\mathrm{flat})}$, with results from simulations (squares) and from our scaling framework (dashed and dotted lines). In the limit $\Delta H \ll d^{(\mathrm{flat})}$, ocean stratification is set primarily by vertical diffusion and d approaches $d^{(\mathrm{flat})}$. The stratification distribution in this regime is sketched in the upper-left and lower-left sub-panels for positive Δb and negative Δb, respectively.

The ratio $\Delta H/d^{(\mathrm{flat})}$ indicates how strongly topography affects ocean stratification and circulation. As ΔH increases, d increases for positive Δb and eventually approaches ΔH (red dashed line in Figure 6). In this limit, the stratified layer sits just beneath the topography, with nearly flat isopycnals. In contrast, for negative Δb, d decreases as ΔH increases (blue dotted line in Figure 6). For very large ΔH (lower-right sub-panel of Figure 6), the stratified layer collapses into a thin layer that follows the sloping topography. Although total meridional buoyancy and heat transport are enhanced, they occur within this thin layer, leaving the deep ocean largely isolated from circulation.

For Enceladus and Europa, we calculate $\Delta H/d^{(\mathrm{flat})}$ under different assumptions. For Enceladus, with $\kappa_v = 10^{-7}\ \mathrm{m}^2\,\mathrm{s}^{-1}$ (comparable to molecular diffusivity; Table 2; Soderlund (2019)), $d^{(\mathrm{flat})}$ is sufficiently small that ΔH (assumed to be 15 km) exceeds it by a factor of ~ 6 for positive Δb and by a factor of ~ 2 for negative Δb

10.1029/2025JE009528

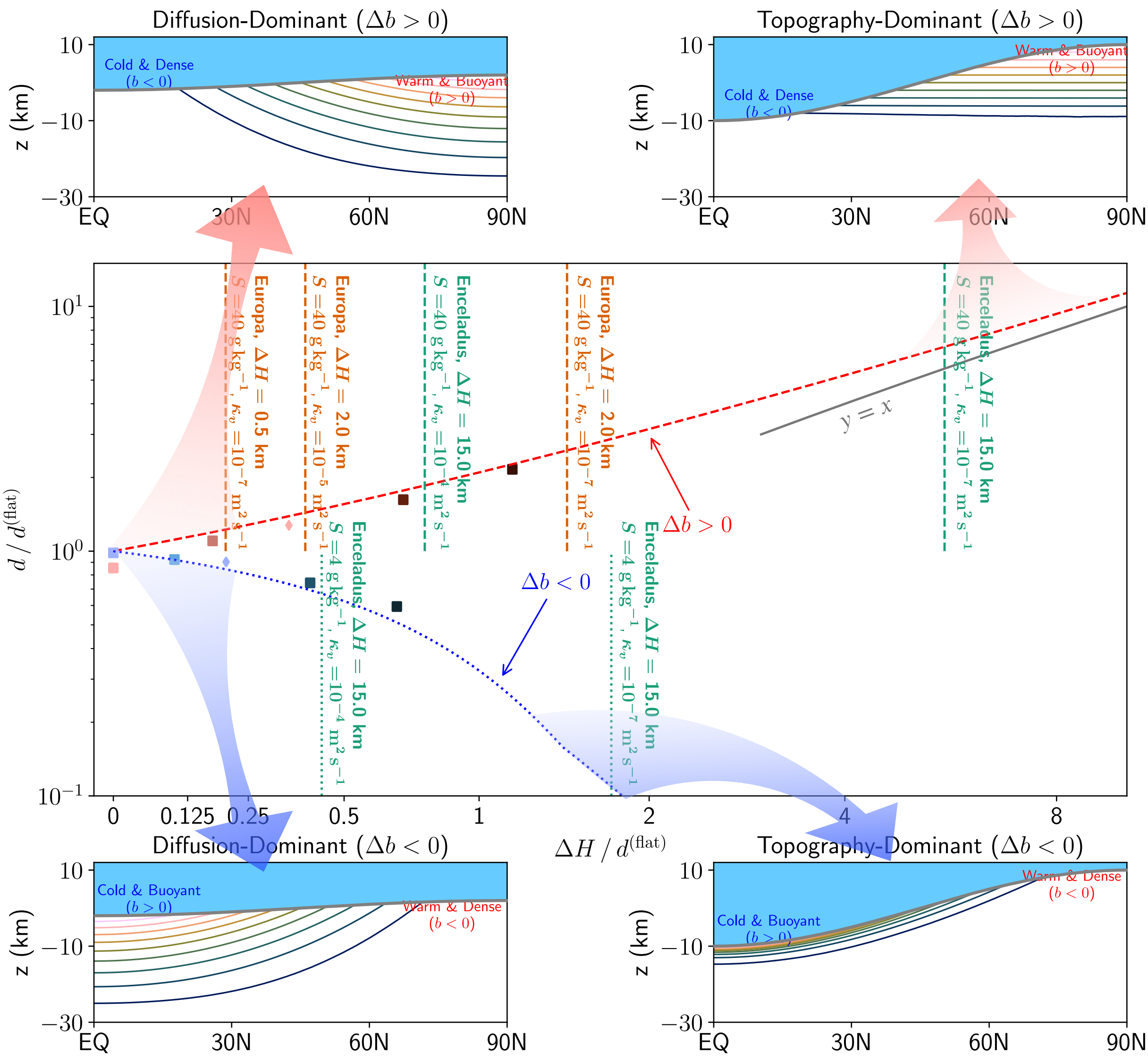

Figure 6. Effect of top topography on ocean stratification. Here, $d^{(\mathrm{flat})}$ is the penetration depth assuming a flat ocean top, computed using the scaling of Kang (2022); Zhang et al. (2024) (which is consistent with this study when $s_{\mathrm{top}} = 0$); d is the actual stratified layer thickness (see Section 6.1 for definitions). Red dashed and blue dotted lines show $d/d^{(\mathrm{flat})}$ as a function of $\Delta H/d^{(\mathrm{flat})}$ for $\Delta b > 0$ and $\Delta b < 0$, respectively. The origin of this buoyancy difference Δb and how α determines its sign are discussed in Section 2.1. The four corner panels show schematics of ocean stratification in four cases: positive versus negative Δb, and diffusion-dominant versus topography-dominant regimes. The lines represent isopycnals (constant buoyancy surfaces): darker lines correspond to denser water, while lighter lines correspond to more buoyant water. These schematics are analytical solutions obtained from Equation 16 of Zhang et al. (2024). When $\Delta H \to 0$, $d \approx d^{(\mathrm{flat})}$, stratification is set by vertical diffusion (upper left and lower left sketches). As ΔH increases, d grows for $\Delta b > 0$ but shrinks for $\Delta b < 0$. In the large $\Delta H/d^{(\mathrm{flat})}$ limit and when $\Delta b > 0$, the stratified layer exists between the minimum and maximum upper topographic depths and the isopycnals are nearly flat (upper right). In contrast when $\Delta b < 0$, the stratified layer becomes thin and hugs the topography (lower right). Vertical lines indicate $\Delta H/d^{(\mathrm{flat})}$ typical of Enceladus and Europa, for given ΔH, ocean salinity S, and vertical diffusivity κ_v. Their vertical position (upper or lower) reflects the sign of Δb set by S, which controls the sign of the thermal expansion coefficient. Salty oceans correspond to the upper part, while fresh oceans correspond to the lower part. Their horizontal position (left or right) depends on the ratio of the diffusion-induced penetration depth to ΔH. Reducing the vertical diffusivity κ_v or increasing ΔH shifts the lines leftward.

(Figure 6). As a result, the stratified layer depth d is about one order of magnitude larger than $d^{(\mathrm{flat})}$ for positive Δb and about one order of magnitude smaller for negative Δb. In this case, the ocean resembles the "topography-dominant" regime (upper and lower right sub-panels). Increasing κ_v to 10^{-4} m^2 s^{-1} (a typical value for the Earth's ocean) reduces $\Delta H/d^{(\mathrm{flat})}$ but keeps it of order unity, so both topography and vertical diffusion become important in setting the stratification and circulation.

Table 2
Parameters of Subsurface Oceans of Icy Moons

	Enceladus	Europa	Titan
a (km)	252	1561	2575
$\Omega\ (\mathrm{s}^{-1})$	5.3×10^{-5}	2.1×10^{-5}	4.6×10^{-6}
$g\ (\mathrm{m\,s^{-2}})$	0.1	1.3	1.4
$\kappa_{\mathrm{mol}}\ (\mathrm{m^2\,s^{-1}})$	1.4×10^{-7}	1.6×10^{-7}	1.8×10^{-7}
$\rho_b\ (10^3\ \mathrm{kg\,m^{-3}})$	1.6	3.0	1.9
D (km)	40	85	369
D_i (km)	20	15	75
T_s (K)	59	110	94
$\Delta b\ (10^{-6}\mathrm{m\,s^{-2}})$	−0.79–0.59	0–30	0–79

Note. Following Soderlund (2019), we show the radius a, bulk density ρ_b, rotation rate Ω, gravitational acceleration g, molecular diffusivity κ_{mol} mean ocean depth D, mean ice thickness D_i, surface temperature T_s, and pole-to-equator under-ice buoyancy difference Δb for Enceladus, Europa, and Titan. To calculate Δb, we first estimate ΔT from Equation 1, assuming $\Delta H = 15$ km for Enceladus and $\Delta H < 2$ km for Europa and Titan, and then substitute it into Equation 3. The thermal expansion coefficient α_T is calculated following the Thermodynamic Equation of Seawater 2010 (McDougall & Barker, 2011), using the pressure beneath the ice shell, $\rho_i g D_i$, assuming hydrostatic balance and salinity ranging between 0 and 40 g kg^{-1}.

For Europa, $\Delta H/d^{(\mathrm{flat})}$ is expected to be smaller. Europa's ΔH is at least an order of magnitude lower than Enceladus' (Nimmo et al., 2007). Assuming $\Delta H = 2$ km and $\kappa_v = 10^{-7}\ \mathrm{m^2\,s^{-1}}$, we obtain $\Delta H/d^{(\mathrm{flat})} \approx 2$, still in the "topography-dominant" regime. However, taking a smaller ΔH (e.g., 0.5 km) or a larger κ_v greatly reduces $\Delta H/d^{(\mathrm{flat})}$, making topography much less important. In Figure 6, we only consider a mean ocean salinity of 40 g kg^{-1} for Europa. This is because a fresher ocean would not change the sign of Δb and thus the overall circulation pattern. Owing to the much higher pressure in Europa's ocean, α becomes negative only when the salinity is smaller than 2 g kg^{-1} (Zeng & Jansen, 2021), a regime that is largely precluded by measurements of Europa's ocean conductivity (Hand & Chyba, 2007).

6.2. Topographic Control on the Upper Limit of Heat Transport

We derive an upper bound on heat transport for the case of positive Δb. Using this bound, we examine the limit $\kappa_v \to 0$, showing that the meridional heat flux vanishes for positive Δb but approaches a finite value for negative Δb. This fundamental difference arises from the underlying energetics.

For positive Δb, we have the following relationship from Equation 13:

$$|\psi^\star| \leq c_s^{-1}\kappa_v/s_{\mathrm{top}} \tag{28}$$

given that $s \geq 0$.

This leads to an upper bound for the meridional heat flux following Equation 27:

$$\mathcal{F}_b \leq c_s^{-1} c_F^{+} \kappa_v \Delta b/s_{\mathrm{top}} \tag{29}$$

A rigorous derivation from the Boussinesq model (Equation 5) is given in Appendix B. This upper bound is based on the fundamental buoyancy flux balance (Section 4.1) and is independent of the dynamics of eddies (Section 4.2).

The above inequality can be converted into an upper bound of the ocean heat transport (OHT in units of W), given our linear equation of state (Equation 2):

$$\mathrm{OHT} \leq (c_s)^{-1} c_F^{+}\left(\pi^2/2\right) a^2 g \kappa_v \rho_w^2 c_p \frac{\mathrm{d}T_{\mathrm{freezing}}}{\mathrm{d}p}, \tag{30}$$

where ρ_w and c_p are the density and heat capacity per mass of seawater; we multiply $\mathcal{F}_b$, the zonal-mean transport, by πa, the average circumference of circles of latitudes, to get the total transport by the three-dimensional flow. Using $\Delta T = \rho_w g \Delta H\left(\mathrm{d}T_{\mathrm{freezing}}/\mathrm{d}p\right)$ and $s_{\mathrm{top}} = \Delta H/((\pi/2)a)$, we find that $\Delta T/s_{\mathrm{top}} = (\pi/2)a\rho_w g\left(\mathrm{d}T_{\mathrm{freezing}}/\mathrm{d}p\right)$, which is independent of ΔH and depends only on the basic parameters of the icy moon. This can be understood from the fact that both ΔT (Equation 1) and s_{top} are proportional to ΔH, which therefore cancels out.

For realistic icy moons, κ_v is highly uncertain because it may depend on complicated ocean tides (Chen et al., 2014; Idini & Nimmo, 2024; Tyler, 2011), convection, and boundary layer processes (Large et al., 1994; Lawrence et al., 2024). The dependence of the freezing point on pressure is constrained by the Clausius-Clapeyron equation, which depends only on the latent heat of fusion and the density difference between water and ice. It gives a freezing point suppression rate of $\mathrm{d}T_{\mathrm{freezing}}/\mathrm{d}p = 8 \times 10^{-8}\ \mathrm{K\,Pa^{-1}}$. If we further assume $\kappa_v = 10^{-4}\ \mathrm{m^2\,s^{-1}}$ (not untypical of the Earth's ocean) and take $\rho_w = 1 \times 10^3\ \mathrm{kg\,m^{-3}}$ and $c_p = 4 \times 10^3\ \mathrm{J\,kg^{-1}\,K^{-1}}$, the upper bound on OHT is 0.5 GW for Enceladus, 235 GW for Europa, and 690 GW for Titan assuming the parameters listed in Table 2. Note that this upper bound only applies to positive Δb, which could be violated by spatial variations in salinity and if α is negative.

This upper bound is reached when κ_v approaches zero. In this limit the isopycnals are all flat, so that there is no available potential energy to drive the ocean circulation. None of our simulations reach this limit (Figure 3). This limit is numerically challenging because small κ_v requires high spatial resolutions and long integration times. In the limit of low diffusivity, our upper bound (Equation 30) can still provide a meaningful constraint on the oceanic meridional heat fluxes.

For negative Δb (corresponding to negative α in Equation 2), the upper bound discussed above is not valid. Instead, our scaling predicts a finite $|\psi^\star|$ (Equation 24) when $s = s_{\text{top}}$. Because the buoyant water source is below the dense water source along the ocean top, the ocean system—resembling rotating Rayleigh-Bénard along a titled surface—still contains available potential energy that can drive ocean circulation.

6.3. Tidal Heat Production, Ocean Stratification, and Ice Shell's Nonsynchronous Rotation

The vertical diffusivity κ_v is a prescribed parameter in both our numerical simulations and scaling analysis. In reality, κ_v reflects a combination of molecular diffusion and turbulent mixing driven by internal tide breaking (Osborn, 1980) and convective plumes (Lecoanet & Quataert, 2013). On Earth, $\kappa_v \sim 10^{-4}\ \text{m}^2\ \text{s}^{-1}$—two to three orders of magnitude larger than molecular diffusivity—primarily due to tidal mixing (Munk & Wunsch, 1998; Wunsch & Ferrari, 2004).

In our calculations, which lack bottom heating and convection, κ_v can be expressed as

$$\kappa_v = \kappa_{\text{mol}} + \Gamma \frac{\epsilon}{\rho_w N^2}, \tag{31}$$

where κ_{mol} is the molecular diffusivity, $\Gamma \sim 0.2$ is the mixing efficiency, N is the buoyancy frequency, $\epsilon = \dot{E}/V$ is the dissipation per unit volume, $\dot{E}$ is the tidal dissipation and V is the ocean volume.

This allows us to reformulate our scaling framework using the tidal dissipation rate $\dot{E}$ as the input parameter, substituting for κ_v via Equation 31. This approach is advantageous because $\dot{E}$ can be directly estimated from tidal dissipation models for icy moon oceans.

Figure 7a shows the OHT as a function of $\dot{E}$. The ratio of OHT to $\dot{E}$ defines a thermal efficiency η, which quantifies how effectively dissipated energy drives heat transport. Following Jansen et al. (2023), $\eta \sim \Gamma c_p/(|\alpha| g D)$, implying that Enceladus, with its low gravity, has a relatively high efficiency, while Titan's stronger gravity leads to a lower η. When $\dot{E}$ is large enough to dominate molecular diffusion, we find a linear relationship between OHT and $\dot{E}$.

Since excessive equatorward OHT can cause net melting at low latitudes and erase the poleward-thinning ice profile, it places an upper bound on the OHT and consequently on the allowable tidal dissipation rate $\dot{E}$. In Figures 7a–7c, the maximum allowed $\dot{E}$ is marked with a point, and a thinner line style is used beyond this point to indicate inconsistency with the observed or assumed ice geometry. The OHT threshold is set equal to $\pi a^2 \mathcal{H}_{\text{cond}}$ where πa^2 is $1/4$ of the surface area of the moon and $\mathcal{H}_{\text{cond}}$ is the estimated conductive heat flux through the equatorial ice:

$$\mathcal{H}_{\text{cond}} = \frac{\kappa_0}{D_i} \log\left(\frac{T_{\text{freezing}}}{T_s}\right) \tag{32}$$

where $\kappa_0 = 651\ \text{W m}^{-1}$ (Petrenko & Whitworth, 1999) is a parameter that determines the thermal conductivity of ice at temperature T, given by $\kappa_{\text{ice}} = \kappa_0/T$; $T_{\text{freezing}} \approx 273\ \text{K}$; D_i is the thickness of the ice shell; T_s is the surface temperature (listed in Table 2). Following Equation 32, the OHT threshold is 8.9 GW for Enceladus, 396 GW for Europa and 223 GW for Titan.

Furthermore, our scaling also predicts equilibrium ocean stratification N^2 as a function of the tidal dissipation rate $\dot{E}$. As shown in Figure 7b, N^2 decreases with increasing $\dot{E}$, since stronger dissipation enhances mixing (Equation 31) and drives the isopycnals farther apart, thus weakening stratification.

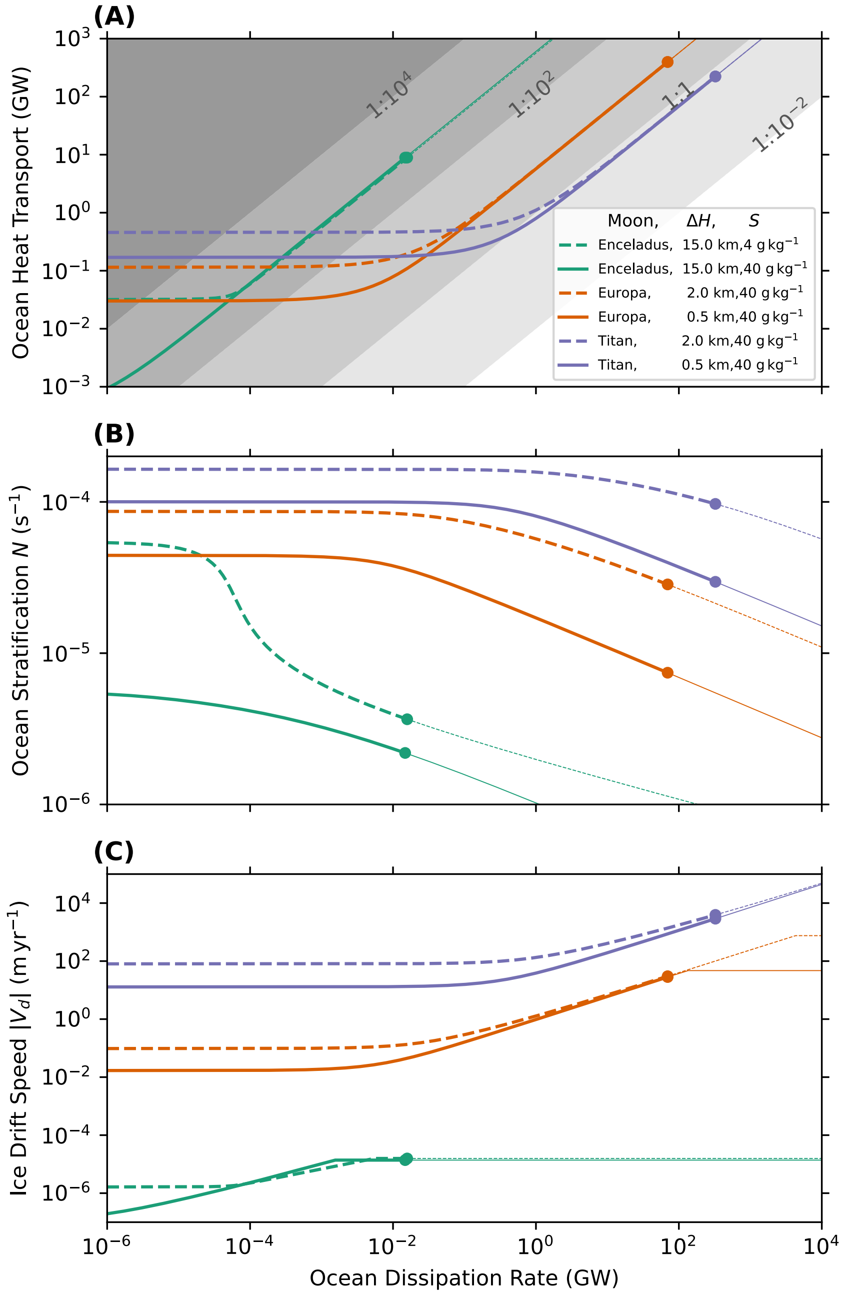

Figure 7. Implication for tidal dissipation, ocean heat transport, ocean stratification, and nonsynchronous rotation of the moon of large-scale ocean circulation. We plot (a) the meridional oceanic heat transport, (b) ocean stratification, and (c) nonsynchronous rotation rate of the ice shell driven by purported large-scale ocean circulation on Enceladus, Europa, and Titan for assumed equator-to-pole ice shell thickness variations ΔH and mean ocean salinities S, as shown in the legend in panel (a). The shading in panel (a) represents the ratio of the y-axis to the x-axis values (thermal efficiency η discussed in Section 6.3). This calculation uses our scaling framework (Equations 24–27) and Equation 31. The parameters assumed for these three icy moons are given in Table 2. For each line, a dot marks the maximum allowed ocean dissipation that is consistent with the observed ice geometry (discussed in Section 7).

In reality, there is a two-way feedback between N^2 and $\dot{E}$. On large scales, ocean stratification is determined by the balance between baroclinic eddies and vertical diffusion (which depends on $\dot{E}$), as captured by our model. However, on a small scale, the generation and dissipation of internal tides are themselves sensitive to N^2 (Auclair-

Desrotour et al., 2018; Idini & Nimmo, 2024; Tyler, 2011). The intersection between our predicted curve $\dot{E}$ - N^2 and those of the tidal dissipation models determines the self-consistent equilibrium value of $\dot{E}$.

Lastly, we predict the speed of nonsynchronous rotation (NSR) of the ice shell driven by thermal wind, following Kang (2024). When the lateral buoyancy gradient near the ocean surface diffuses into the ocean interior, it generates a zonal current (thermal wind), the strength of which depends on the meridional buoyancy gradient and the depth over which it penetrates. The resulting velocity difference across the vertical extent is given by:

$$\Delta_v U = \frac{\Delta b}{8a\Omega} \min\{as, D\}. \tag{33}$$

where D is the depth of the ocean, which sets an upper bound on the depth of penetration. This zonal flow exerts a frictional stress on the overlying ice shell:

$$\tau_s = (1/4)\rho_w C_d |\Delta_v U| \Delta_v U, \tag{34}$$

where C_d is the drag coefficient, taken to be 5×10^{-3} in this study, which is broadly consistent with observed ice-ocean drag coefficients (Lu et al., 2011). This stress imparts a torque on the ice shell, leading to NSR at a drift speed (Ashkenazy et al., 2023):

$$V_d = k_0 G^2 \frac{\rho_b^2 a^2}{\eta_{\text{ice}} \Omega^4 D_i} \tau_s \left(1 - \frac{2\phi_{\text{TC}} + \sin(2\phi_{\text{TC}})}{\pi}\right) \tag{35}$$

where $k_0 = \frac{5\pi^3}{36}\frac{5+\nu}{1+\nu}\frac{1}{(1+k_f)^2}$, with the Poisson ratio $\nu = 1/3$ and the fluid Love number $k_f = 1.5$; G is the gravitational constant; ρ_b is the bulk density of the moon; the drag coefficient C_d is assumed to be 5×10^{-3}; ϕ_{TC} is the latitude at which the tangent cylinder intersects with the ice; η_{ice} is the depth-averaged viscosity of the ice shell, assumed to be 1×10^{15} Pa s (Kang (2024) contains a typo under Equation 8: the default η_{ice} is 10^{15} Pa s rather than 10^{16} Pa s). Figure 7c shows the relationship between ocean dissipation $\dot{E}$ and drift speed $|V_d|$. As dissipation increases, the thermal wind penetrates deeper, strengthening the zonal flow, and thus the NSR, until the penetration depth reaches the full ocean depth. The drift speed V_d, which may be measurable by future missions, could provide constraints on both oceanic circulation and tidal dissipation.

With our scaling framework, we unify several seemingly independent processes through the lens of large-scale ocean circulation—including ice shell geometry, oceanic tidal dissipation, heat flux through the ice, and even the non-synchronous rotation of the moon. This connection offers a pathway to better constrain oceanic parameters and enables cross-validation between independent observations. In the near future, Europa Clipper and JUICE (JUpiter ICy Moons Explorer) will visit Europa, Ganymede, and Callisto, providing improved measurements of non-synchronous rotation rates and ice thickness profiles. These observations can, in turn, be translated into constraints on the oceanic dissipation rate $\dot{E}$ and stratification N^2 using the analysis presented here. Once N^2 is known, the tidal response of the ocean can be calculated from first principles (Hay & Matsuyama, 2019; Rovira-Navarro et al., 2019; Rekier et al., 2019; Tyler, 2020) and potentially compared with future seismic data, when available.

7. Discussion and Conclusions

This study investigates ocean circulation on icy moons driven by under-ice temperature gradients arising from spatially varying ice shell thickness. Motivated by the fact that tidal dissipation tends to be polar-amplified, we consider a poleward-thinning ice shell following a cosine profile. The Clausius-Clapeyron relation implies that the water beneath thicker equatorial ice is colder than the water beneath the poles. Depending on the mean salinity and pressure of the ocean, the thermal expansion coefficient α can be positive or negative, determining whether the equatorial or polar water is denser.

Building on Zhang et al. (2024) and Kang (2022), we derive scaling laws for circulation strength and heat transport, incorporating the effects of ice topography and negative α. We tested these predictions with 26 or so numerical simulations, exploring how topographic slope, vertical diffusivity, and buoyancy forcing influence ocean stratification and heat transport.

Our main conclusions are as follows.

1. *Circulation structure*: Vertical diffusion energizes baroclinic eddies that can be represented as an overturning cell. This cell sinks at the equator when $\alpha > 0$ and at the poles when $\alpha < 0$. Regardless of the direction, heat flows from the poles (thin ice) toward the equator (thick ice), consistent with Kang, Mittal, et al. (2022).
2. *Topographic suppression at positive* α: When $\alpha > 0$, the topography elevates the buoyant polar water above the denser equatorial water, weakening polar stratification and reducing meridional transport.
3. *Topographic enhancement at negative* α: When $\alpha < 0$, topography lifts dense polar water above buoyant equatorial water, increasing the available potential energy (Jansen et al., 2023), thinning the stratified layer and enhancing heat transport. In this case, the heat flux remains finite even as $\kappa_v \to 0$.
4. *Topography-dominant regime at small* κ_v *and large* ΔH: Topographic variations control ocean stratification and circulation when the topographic height difference exceeds the penetration depth set by vertical diffusion. In this regime, for positive Δb, the stratified layer conforms beneath the topography, with nearly flat isopycnals, leading to a weakened overall circulation. For negative Δb, the stratified layer forms a thin sheet that hugs the sloped topography. In both cases, the overturning circulation does not penetrate the abyssal ocean.

Finally, there are important caveats to our study. First, we do not account for salinity variations, which can arise from melting and refreezing processes at the ice-ocean interface (Ashkenazy et al., 2018; Kang, Mittal, et al., 2022; Lobo et al., 2021). These processes can make the water saltier near the poles and fresher near the equator. For positive α_T, the buoyancy difference due to temperature is reduced; for negative α_T, it is enhanced, thereby modifying the strength of the eddy-driven overturning. Near the salinity at which α_T switches sign (0–24 $\mathrm{g\,kg^{-1}}$, depending on pressure), salinity variations may strongly influence the strength of the meridional buoyancy gradient and may even reverse its sign. This effect is discussed in Kang and Zhang (2026). Second, we neglect bottom heating (Bire et al., 2022, 2023; Bouffard et al., 2025; Goodman & Lenferink, 2012; Goodman et al., 2004; Lemasquerier et al., 2023; Melosh et al., 2004; Sekine et al., 2015; Soderlund et al., 2014; Soderlund, 2019; Zeng & Jansen, 2021), which may influence ocean stratification and, through redistribution of heat, also affect the geometry of the overlying ice shell. For positive α, convective heat fluxes are shown in numerical simulations of convective plume penetration to concentrate toward the equator, melting ice there (Kang, 2023; Wang et al., 2026). Finally, our simulations are conducted in a Cartesian coordinate system, rather than a more realistic spherical geometry. This simplification may modify predicted quantities, such as the isopycnal slope, meridional heat transport, and the depth of the ocean's stratified layer, by a constant factor. However, we prefer to use Cartesian coordinates because it enables us to deploy ultra fast numerical schemes on GPUs.

Appendix A: Scaling for Isopycnal Slope

At equilibrium, vertical heat diffusion and eddy heat transport balance one-another:

$$\partial_z\left(\kappa_v \partial_z \overline{b}\right) - \partial_y\left(\psi^\star \partial_z \overline{b}\right) + \partial_z\left(\psi^\star \partial_y \overline{b}\right) = 0. \tag{A1}$$

where $\psi^\star$ is the eddy-driven overturning streamfunction (shading in Figure 3).

We consider its weak form:

$$\int_D \left(\partial_z\left(\kappa_v\left(\partial_z \overline{b}\right)\right) - \partial_y\left(\psi^\star \partial_z \overline{b}\right) + \partial_z\left(\psi^\star \partial_y \overline{b}\right)\right)\phi \,\mathrm{d}y\,\mathrm{d}z = 0, \tag{A2}$$

where $\phi(y,z)$ is a test function; $\mathcal{D}$ is the Northern Hemisphere of the ocean domain of (y,z).

We perform integration by parts and use Green's theorem:

$$\int_{\partial\mathcal{D}} \left(\left(-\phi\psi^\star \partial_z \overline{b} \right) \mathrm{d}z + \left(\phi\psi^\star \partial_y \overline{b} + \kappa_v \phi \partial_z \overline{b} \right) \mathrm{d}y \right) + \int_{\mathcal{D}} \left(-\kappa_v \partial_z \overline{b} \partial_z \phi + \psi^\star \partial_z \overline{b} \partial_y \phi - \psi^\star \partial_y \overline{b} \partial_z \phi \right) \mathrm{d}y \, \mathrm{d}z = 0. \tag{A3}$$

where $\partial\mathcal{D}$ is the boundary of $\mathcal{D}$.

The contour integration term vanishes if we choose $\phi = z - z_{\mathrm{top}}$. Along the upper boundary, $\phi = 0$; $\psi = 0$ at the equator and the North Pole; $\left(-\kappa_v \partial_z \overline{b} - \psi^\star \partial_y \overline{b}\right)$ is the net vertical buoyancy flux, which is zero as we do not consider heating from below in this study.

For $\phi = z - z_{\mathrm{top}}$, $\partial_y \phi = -s_{\mathrm{top}}$ and $\partial_z \phi = 1$. Thus, Equation A3 becomes:

$$\int_{\mathcal{D}} \partial_z \overline{b} \left(-\kappa_v + \psi^\star \left(\tilde{s} - s_{\mathrm{top}} \right) \right) \mathrm{d}y \, \mathrm{d}z = 0, \tag{A4}$$

where $\tilde{s} = -\partial_y \overline{b} / \partial_z \overline{b}$ is the signed isopycnal slope. The isopycnal slope we represent in the main text is the absolute value $s = |\tilde{s}|$. For positive Δb, $\tilde{s} < 0$ and $\psi^\star < 0$ in the Northern Hemisphere; For negative Δb, $\tilde{s} > 0$ and $\psi^\star > 0$ instead. Taking into account the signs of $\tilde{s}$ and $\psi^\star$, we get

$$\int_{\mathcal{D}} \partial_z \overline{b} \left(-\kappa_v + |\psi^\star| \left(s + \mathrm{sgn}(\Delta b) s_{\mathrm{top}} \right) \right) \mathrm{d}y \, \mathrm{d}z = 0, \tag{A5}$$

which is a more rigorous form of Equation 13.

The above derivation has a clear physical interpretation. Equation A2 represents the buoyancy transport budget in the direction of the gradient of ψ. For the choice $\phi = z - z_{\mathrm{top}}$, the gradient of ψ becomes $-s_{\mathrm{top}}\,\mathbf{j} + \mathbf{k}$, which is perpendicular to the upper boundary surface. The total buoyancy transport in this direction, including both diffusive flux and eddy transport, must vanish; otherwise, the global-mean buoyancy would change over time.

Appendix B: Upper Bound on the Heat Flux for Positive α

The upper bound of the heat flux can be derived from the buoyancy budget. The steady-state buoyancy equation integrated over the domain gives the following:

$$\partial_z \overline{wb} + \partial_y \overline{vb} - \partial_z \left(\kappa_v \partial_z \overline{b} \right) - \partial_y \left(\kappa_h \partial_y \overline{b} \right) = 0, \tag{B1}$$

where buoyancy transport by Eulerian overturning and horizontal diffusion is also included. Similarly to Appendix A, we seek the weak form using $(z - z_{\mathrm{top}})$ as the test function:

$$\int_{\mathcal{D}} (z - z_{\mathrm{top}}) \left(\partial_z \overline{wb} + \partial_y \overline{vb} - \partial_z \left(\kappa_v \partial_z \overline{b} \right) - \partial_y \left(\kappa_h \partial_y \overline{b} \right) \right) \mathrm{d}y \, \mathrm{d}z = 0 \tag{B2}$$

where $\mathcal{D}$ is the Northern Hemisphere where $y \in [0, (\pi/2)a]$ and $z \in [-D, z_{\mathrm{top}}(y)]$.

We integrate the equation by part. Using the no-flux boundary condition at the meridional and bottom boundaries, the contour integration term vanishes:

$$\int_{\mathcal{D}} \left(-\overline{wb} - s_{\mathrm{top}} \overline{vb} + \kappa_v \partial_z \overline{b} + s_{\mathrm{top}} \kappa_h \partial_y \overline{b} \right) \mathrm{d}y \, \mathrm{d}z = 0. \tag{B3}$$

We separate the terms for the horizontal transport and get a relation between the net horizontal transport weighted by s_{top} and the vertical transport:

$$\mathcal{F}_b = \frac{1}{\Delta H}\left(\int_D \kappa_v \partial_z \overline{b} \mathrm{d}y\,\mathrm{d}z - \int_D \overline{wb} \mathrm{d}y\,\mathrm{d}z\right) \tag{B4}$$

where $\mathcal{F}_b$ is the vertical integrated meridional buoyancy transport averaged with a weight of s_{top}:

$$\mathcal{F}_b = \frac{\int_D s_{\text{top}}\left(\overline{vb} - \kappa_h \partial_y \overline{b}\right) \mathrm{d}y\,\mathrm{d}z}{\int_0^{(\pi/2)a} s_{\text{top}} \mathrm{d}y}. \tag{B5}$$

Here, we have used $\int_0^{(\pi/2)a} s_{\text{top}} \mathrm{d}y = \Delta H$.

The vertical diffusion term is bounded by:

$$\int_D \kappa_v \partial_z \overline{b} \mathrm{d}y\,\mathrm{d}z \leq \kappa_v((\pi/2)a)|\Delta b| \tag{B6}$$

where $(\pi/2)a$ is the horizontal extent of $\mathcal{D}$.

The vertical buoyancy flux $\overline{wb}$, the rate at which the potential energy is released and drives the circulation, must be nonnegative:

$$\int_D \overline{wb} \mathrm{d}y\,\mathrm{d}z \leq 0 \tag{B7}$$

Combining Equations B5–B7, we get:

$$\mathcal{F}_b \leq \frac{(\pi/2)a}{\Delta H}\kappa_v |\Delta b|, \tag{B8}$$

which is a more rigorous form of Equation 29.

Conflict of Interest

The authors declare no conflicts of interest relevant to this study.

Availability Statement

Data and scripts used for data analysis are available online at https://doi.org/10.5281/zenodo.17871903.

Acknowledgments
This project uses Oceananigans (https://github.com/CliMA/Oceananigans.jl), an open source ocean general circulation model. The authors thank Simone Silvestri, Gregory L. Wagner, and Xin Kai Lee for technical support for Oceananigans and Yuchen Ma, Shuang Wang, Wenda Zhang, and Kaushal Gianchandni for helpful discussions. This work was supported in part by NASA Astrobiology Grant 80NSSC19K1427 "Exploring Ocean Worlds".

References

Ames, F., Ferreira, D., Czaja, A., & Masters, A. (2025). Ocean stratification impedes particulate transport to the plumes of enceladus. *Communications Earth & Environment*, *6*(1), 63. https://doi.org/10.1038/s43247-025-02036-3

Arakawa, A., & Lamb, V. R. (1977). Computational design of the basic dynamical processes of the ucla general circulation model. *General circulation models of the atmosphere*, *17*, 173–265. https://doi.org/10.1016/B978-0-12-460817-7.50009-4

Ashkenazy, Y., Sayag, R., & Tziperman, E. (2018). Dynamics of the global meridional ice flow of Europa's icy shell. *Nature Astronomy*, *2*(1), 43–49. https://doi.org/10.1038/s41550-017-0326-7

Ashkenazy, Y., & Tziperman, E. (2021). Dynamic Europa ocean shows transient taylor columns and convection driven by ice melting and salinity. *Nature Communications*, *12*(1), 1–12. https://doi.org/10.1038/s41467-021-26710-0

Ashkenazy, Y., Tziperman, E., & Nimmo, F. (2023). Non-synchronous rotation on europa driven by ocean currents. *AGU Advances*, *4*(3), e2022AV000849. https://doi.org/10.1029/2022AV000849

Auclair-Desrotour, P., Mathis, S., Laskar, J., & Leconte, J. (2018). Oceanic tides from earth-like to ocean planets. *Astronomy & Astrophysics*, *615*, A23. https://doi.org/10.1051/0004-6361/201732249

Beuthe, M. (2018). Enceladus's crust as a non-uniform thin shell: I tidal deformations. *Icarus*, *302*, 145–174. https://doi.org/10.1016/j.icarus.2017.11.009

Bire, S., Kang, W., Ramadhan, A., Campin, J.-M., & Marshall, J. (2022). Exploring ocean circulation on icy moons heated from below. *Journal of Geophysical Research: Planets*, *127*(3), e2021JE007025. https://doi.org/10.1029/2021je007025

Bire, S., Mittal, T., Kang, W., Ramadhan, A., Tuckman, P. J., German, C. R., et al. (2023). Divergent behavior of hydrothermal plumes in fresh versus salty icy ocean worlds. *Journal of Geophysical Research: Planets*, *128*(11), e2023JE007740. https://doi.org/10.1029/2023JE007740

Bouffard, M., Choblet, G., Amit, H., Tobie, G., Čadek, O., & Terra-Nova, F. (2025). Seafloor hydrothermal control over ocean dynamics in enceladus. *Nature Astronomy*, *9*(5), 1–8. https://doi.org/10.1038/s41550-025-02490-1

Čadek, O., Tobie, G., Van Hoolst, T., Massé, M., Choblet, G., Lefèvre, A., et al. (2016). Enceladus's internal ocean and ice shell constrained from Cassini gravity, shape, and libration data. *Geophysical Research Letters*, *43*(11), 5653–5660. https://doi.org/10.1002/2016GL068634

Carr, M. H., Belton, M. J., Chapman, C. R., Davies, M. E., Geissler, P., Greenberg, R., et al. (1998). Evidence for a subsurface ocean on europa. *Nature*, *391*(6665), 363–365. https://doi.org/10.1038/34857

Charney, J. G., & Stern, M. E. (1962). On the stability of internal baroclinic jets in a rotating atmosphere. *Journal of the Atmospheric Sciences*, *19*(2), 159–172. https://doi.org/10.1175/1520-0469(1962)019<0159:OTSOIB>2.0.CO;2

Chen, E. M. A., Nimmo, F., & Glatzmaier, G. A. (2014). Tidal heating in icy satellite oceans. *Icarus*, *229*, 11–30. https://doi.org/10.1016/j.icarus.2013.10.024

Chyba, C. F. (2000). Energy for microbial life on europa. *Nature*, *403*(6768), 381–382. https://doi.org/10.1038/35000281

Dellar, P. J. (2011). Variations on a beta-plane: Derivation of non-traditional beta-plane equations from hamilton's principle on a sphere. *Journal of Fluid Mechanics*, *674*, 174–195. https://doi.org/10.1017/S0022112010006464

Gallet, B., & Ferrari, R. (2021). A quantitative scaling theory for meridional heat transport in planetary atmospheres and oceans. *AGU Advances*, *2*(3), e2020AV000362. https://doi.org/10.1029/2020av000362

Galperin, B., Sukoriansky, S., & Dikovskaya, N. (2008). Zonostrophic turbulence. *Physica Scripta*, *2008*(T132), 014034. https://doi.org/10.1088/0031-8949/2008/t132/014034

Gent, P. R., & Mcwilliams, J. C. (1990). Isopycnal mixing in ocean circulation models. *Journal of Physical Oceanography*, *20*(1), 150–155. https://doi.org/10.1175/1520-0485(1990)020<0150:imiocm>2.0.co;2

Glein, C. R., & Waite, J. H. (2020). The Carbonate geochemistry of enceladus' Ocean. *GRL*, *47*(3), 591. https://doi.org/10.1029/2019gl085885

Goodman, J. C., Collins, G. C., Marshall, J., & Pierrehumbert, R. T. (2004). Hydrothermal plume dynamics on Europa: Implications for chaos formation. *Journal of Geophysical Research*, *109*(E3). https://doi.org/10.1029/2003JE002073

Goodman, J. C., & Lenferink, E. (2012). Numerical simulations of marine hydrothermal plumes for europa and other icy worlds. *Icarus*, *221*(2), 970–983. https://doi.org/10.1016/j.icarus.2012.08.027

Grimshaw, R. H. J. (1975). A note on the β-plane approximation. *Tellus*, *27*(4), 351–357. https://doi.org/10.1111/j.2153-3490.1975.tb01685.x

Hand, K., & Chyba, C. (2007). Empirical constraints on the salinity of the europan ocean and implications for a thin ice shell. *Icarus*, *189*(2), 424–438. https://doi.org/10.1016/j.icarus.2007.02.002

Hay, H. C. F. C., & Matsuyama, I. (2019). Nonlinear tidal dissipation in the subsurface oceans of Enceladus and other icy satellites. *Icarus*, *319*, 68–85. https://doi.org/10.1016/j.icarus.2018.09.019

Heimpel, M., & Aurnou, J. (2007). Turbulent convection in rapidly rotating spherical shells: A model for equatorial and high latitude jets on jupiter and saturn. *Icarus*, *187*(2), 540–557. https://doi.org/10.1016/j.icarus.2006.10.023

Held, I. M., & Larichev, V. D. (1996). A scaling theory for horizontally homogeneous, baroclinically unstable flow on a beta plane. *JAS*, *53*(7), 946–952. https://doi.org/10.1175/1520-0469(1996)053<0946:astfhh>2.0.co;2

Hemingway, D. J., & Mittal, T. (2019). Enceladus's ice shell structure as a window on internal heat production. *Icarus*, *332*, 111–131. https://doi.org/10.1016/j.icarus.2019.03.011

Idini, B., & Nimmo, F. (2024). Resonant stratification in titan's global ocean. *The Planetary Science Journal*, *5*(1), 15. https://doi.org/10.3847/PSJ/ad11ef

Ito, T., & Marshall, J. (2008). Control of lower-limb overturning circulation in the southern ocean by diapycnal mixing and mesoscale eddy transfer. *Journal of Physical Oceanography*, *38*(12), 2832–2845. https://doi.org/10.1175/2008jpo3878.1

Jansen, M. F., Kang, W., Kite, E. S., & Zeng, Y. (2023). Energetic constraints on ocean circulations of icy ocean worlds. *The Planetary Science Journal*, *4*(6), 117. https://doi.org/10.3847/PSJ/acda95

Kang, W. (2022). Different ice-shell geometries on Europa and Enceladus due to their different sizes: Impacts of ocean heat trans. *The Astrophysical Journal*, *934*(2), 116. https://doi.org/10.3847/1538-4357/ac779c

Kang, W. (2023). The modulation effect of ice thickness variations on convection in icy ocean worlds. *Monthly Notices of the Royal Astronomical Society*, *525*(4), 5251–5261. https://doi.org/10.1093/mnras/stad2638

Kang, W. (2024). Nonsynchronous rotation of icy moon ice shells: The thermal wind perspective. *Science Advances*, *10*(4), eadk2277. https://doi.org/10.1126/sciadv.adk2277

Kang, W., & Flierl, G. (2020). Spontaneous formation of geysers at only one pole on enceladus's ice shell. *Proceedings of the National Academy of Sciences*, *117*(26), 14764–14768. https://doi.org/10.1073/pnas.2001648117

Kang, W., & Jansen, M. (2022). On icy ocean worlds, size controls ice shell geometry. *The Astrophysical Journal*, *935*(2), 103. https://doi.org/10.3847/1538-4357/ac7a32

Kang, W., Marshall, J., Mittal, T., & Bire, S. (2022). Ocean dynamics and tracer transport over the south pole geysers of enceladus. *MNRAS*, *517*(3), 3485–3494. https://doi.org/10.1093/mnras/stac2882

Kang, W., Mittal, T., Bire, S., Campin, J.-M., & Marshall, J. (2022). How does salinity shape ocean circulation and ice geometry on Enceladus and other icy satellites? *Science Advances*, *8*(29), eabm4665. https://doi.org/10.1126/sciadv.abm4665

Kang, W., & Zhang, Y. (2026). Subsurface ocean salinity and dissipation rate inferred from Enceladus ice shell morphology. *arXiv preprint arXiv: 2603.22602*. https://doi.org/10.48550/arXiv.2603.22602

Khurana, K., Kivelson, M., Stevenson, D., Schubert, G., Russell, C., Walker, R., & Polanskey, C. (1998). Induced magnetic fields as evidence for subsurface oceans in europa and callisto. *Nature*, *395*(6704), 777–780. https://doi.org/10.1038/27394

Kivelson, M. G., Khurana, K. K., Russell, C. T., Volwerk, M., Walker, R. J., & Zimmer, C. (2000). Galileo magnetometer measurements: A stronger case for a subsurface ocean at europa. *Science*, *289*(5483), 1340–1343. https://doi.org/10.1126/science.289.5483.1340

Large, W. G., McWilliams, J. C., & Doney, S. C. (1994). Oceanic vertical mixing: A review and a model with a nonlocal boundary layer parameterization. *Reviews of Geophysics*, *32*(4), 363–403. https://doi.org/10.1029/94RG01872

Lawrence, J., Schmidt, B., Buffo, J., Washam, P., Chivers, C., & Miller, S. (2024). Ice-ocean interactions on ocean worlds influence ice shell topography. *Journal of Geophysical Research: Planets*, *129*(2), e2023JE008036. https://doi.org/10.1029/2023JE008036

Le, H., & Moin, P. (1991). An improvement of fractional step methods for the incompressible navier-stokes equations. *Journal of Computational Physics*, *92*(2), 369–379. https://doi.org/10.1016/0021-9991(91)90215-7

Lecoanet, D., & Quataert, E. (2013). Internal gravity wave excitation by turbulent convection. *Monthly Notices of the Royal Astronomical Society*, *430*(3), 2363–2376. https://doi.org/10.1093/mnras/stt055

Lemasquerier, D. G., Bierson, C. J., & Soderlund, K. M. (2023). Europa's ocean translates interior tidal heating patterns to the ice-ocean boundary. *AGU Advances*, *4*(6), e2023AV000994. https://doi.org/10.1029/2023AV000994

Lobo, A. H., Thompson, A. F., Vance, S. D., & Tharimena, S. (2021). A pole-to-equator ocean overturning circulation on enceladus. *Nature Geoscience*, *14*(4), 185–189. https://doi.org/10.1038/s41561-021-00706-3

Lu, P., Li, Z., Cheng, B., & Leppäranta, M. (2011). A parameterization of the ice-ocean drag coefficient. *Journal of Geophysical Research*, *116*(C7). https://doi.org/10.1029/2010jc006878

Marshall, J., & Radko, T. (2003). Residual-mean solutions for the Antarctic Circumpolar Current and its associated overturning circulation. *Journal of Physical Oceanography*, *33*(11), 2341–2354. https://doi.org/10.1175/1520-0485(2003)033<2341:RSFTAC>2.0.CO;2

McDougall, T. J., & Barker, P. M. (2011). Getting started with teos-10 and the Gibbs seawater (gsw) oceanographic toolbox. *SCOR/IAPSO WG*, *127*, 1–28.

McKinnon, W., & Schenk, P. (2021). A new global topographic map of enceladus: Geophysical considerations. *Agu fall meeting abstracts*, *2021*, P35C–2141. Retrieved from https://ui.adsabs.harvard.edu/abs/2021AGUFM.P35C2141M

Mechoso, C. R. (1980). Baroclinic instability of flows along sloping boundaries. *Journal of the Atmospheric Sciences*, *37*(6), 1393–1399. https://doi.org/10.1175/1520-0469(1980)037<1393:biofas>2.0.co;2

Melosh, H., Ekholm, A., Showman, A., & Lorenz, R. (2004). The temperature of Europa's subsurface water ocean. *Icarus*, *168*(2), 498–502. https://doi.org/10.1016/j.icarus.2003.11.026

Mittal, R., & Iaccarino, G. (2005). Immersed boundary methods. *Annual Review of Fluid Mechanics*, *37*(1), 239–261. https://doi.org/10.1146/annurev.fluid.37.061903.175743

Munk, W., & Wunsch, C. (1998). Abyssal recipes ii: Energetics of tidal and wind mixing. *Deep-sea Research Part I-oceanographic Research Papers*, *45*(12), 1977–2010. https://doi.org/10.1016/s0967-0637(98)00070-3

Nimmo, F., Thomas, P., Pappalardo, R., & Moore, W. (2007). The global shape of Europa: Constraints on lateral shell thickness variations. *Icarus*, *191*(1), 183–192. https://doi.org/10.1016/j.icarus.2007.04.021

Ojakangas, G. W., & Stevenson, D. J. (1989). Thermal state of an ice shell on europa. *Icarus*, *81*(2), 220–241. https://doi.org/10.1016/0019-1035(89)90052-3

Osborn, T. R. (1980). Estimates of the local rate of vertical diffusion from dissipation measurements. *Journal of Physical Oceanography*, *10*(1), 83–89. https://doi.org/10.1175/1520-0485(1980)010<0083:eotlro>2.0.co;2

Pappalardo, R. T., Belton, M. J., Breneman, H., Carr, M., Chapman, C. R., Collins, G., et al. (1999). Does europa have a subsurface ocean? Evaluation of the geological evidence. *JGR: Planets*, *104*(E10), 24015–24055. https://doi.org/10.1029/1998je000628

Petrenko, V., & Whitworth, R. (1999). *Physics of ice*. OUP.

Plumb, R. A., & Ferrari, R. (2005). Transformed eulerian-mean theory. part i: Nonquasigeostrophic theory for eddies on a zonal-mean flow. *Journal of Physical Oceanography*, *35*(2), 165–174. https://doi.org/10.1175/JPO-2669.1

Ramadhan, A., Wagner, G., Hill, C., Campin, J.-M., Churavy, V., Besard, T., et al. (2020). Oceananigans. jl: Fast and friendly geophysical fluid dynamics on GPUs. *Journal of Open Source Software*, *5*(53), 2018. https://doi.org/10.21105/joss.02018

Rekier, J., Trinh, A., Triana, S., & Dehant, V. (2019). Internal energy dissipation in enceladus's subsurface ocean from tides and libration and the role of inertial waves. *Journal of Geophysical Research: Planets*, *124*(8), 2198–2212. https://doi.org/10.1029/2019je005988

Rhines, P. B. (1975). Waves and turbulence on a beta-plane. *Journal of Fluid Mechanics*, *69*(3), 417–443. https://doi.org/10.1017/s0022112075001504

Rhines, P. B. (1979). Geostrophic turbulence. *Annual Review of Fluid Mechanics*, *11*(1), 401–441. https://doi.org/10.1146/annurev.fl.11.010179.002153

Rovira-Navarro, M., Rieutord, M., Gerkema, T., Maas, L. R., van der Wal, W., & Vermeersen, B. (2019). Do tidally-generated inertial waves heat the subsurface oceans of Europa and Enceladus? *Icarus*, *321*, 126–140. https://doi.org/10.1016/j.icarus.2018.11.010

Russell, M. J., Murray, A. E., & Hand, K. P. (2017). The possible emergence of life and differentiation of a shallow biosphere on irradiated icy worlds: The example of europa. *Astrobiology*, *17*(12), 1265–1273. https://doi.org/10.1089/ast.2016.1600

Sekine, Y., Shibuya, T., Postberg, F., Hsu, H.-W., Suzuki, K., Masaki, Y., et al. (2015). High-temperature water–rock interactions and hydrothermal environments in the chondrite-like core of enceladus. *Nature Communications*, *6*(1), 8604. https://doi.org/10.1038/ncomms9604

Shu, C.-W. (2009). High order weighted essentially nonoscillatory schemes for convection dominated problems. *SIAM Review*, *51*(1), 82–126. https://doi.org/10.1137/070679065

Silvestri, S., Wagner, G. L., Campin, J.-M., Constantinou, N. C., Hill, C. N., Souza, A., & Ferrari, R. (2024). A new WENO-based momentum advection scheme for simulations of ocean mesoscale turbulence. *Journal of Advances in Modeling Earth Systems*, *16*(7), e2023MS004130. https://doi.org/10.1029/2023MS004130

Silvestri, S., Wagner, G. L., Constantinou, N. C., Hill, C. N., Campin, J.-M., Souza, A. N., et al. (2025). A GPU-based ocean dynamical core for routine mesoscale-resolving climate simulations. *Journal of Advances in Modeling Earth Systems*, *17*(4), e2024MS004465. https://doi.org/10.1029/2024MS004465

Soderlund, K., Schmidt, B., Wicht, J., & Blankenship, D. (2014). Ocean-driven heating of Europa's icy shell at low latitudes. *Nature Geoscience*, *7*(1), 16–19. https://doi.org/10.1038/ngeo2021

Soderlund, K. M. (2019). Ocean dynamics of outer solar system satellites. *Geophysical Research Letters*, *46*(15), 8700–8710. https://doi.org/10.1029/2018gl081880

Tajeddine, R., Soderlund, K. M., Thomas, P. C., Helfenstein, P., Hedman, M. M., Burns, J. A., & Schenk, P. M. (2017). True polar wander of Enceladus from topographic data. *Icarus*, *295*, 46–60. https://doi.org/10.1016/j.icarus.2017.04.019

Taubner, R.-S., Pappenreiter, P., Zwicker, J., Smrzka, D., Pruckner, C., Kolar, P., et al. (2018). Biological methane production under putative enceladus-like conditions. *Nature comm.*, *9*(1), 1–11. https://doi.org/10.1038/s41467-018-02876-y

Thomas, P., Tajeddine, R., Tiscareno, M., Burns, J., Joseph, J., Loredo, T., et al. (2016). Enceladus's measured physical libration requires a global subsurface ocean. *Icarus*, *264*, 37–47. https://doi.org/10.1016/j.icarus.2015.08.037

Tyler, R. (2011). Tidal dynamical considerations constrain the state of an ocean on Enceladus. *Icarus*, *211*(1), 770–779. https://doi.org/10.1016/j.icarus.2010.10.007

Tyler, R. H. (2020). Heating of enceladus due to the dissipation of ocean tides. *Icarus*, *348*, 113821. https://doi.org/10.1016/j.icarus.2020.113821

Wang, S., Kang, W., & Li, C. (2026). A tug-of-war between baroclinic eddies and convection: Implications for icy moon oceans. *arXiv preprint arXiv:2603.17185*. https://doi.org/10.48550/arXiv.2603.17185

Weber, J. M., Marlin, T. C., Prakash, M., Teece, B. L., Dzurilla, K., & Barge, L. M. (2023). A review on hypothesized metabolic pathways on europa and enceladus: Space-flight detection considerations. *Life*, *13*(8), 1726. https://doi.org/10.3390/life13081726
Wunsch, C., & Ferrari, R. (2004). Vertical mixing, energy and thegeneral circulation of the oceans. *Annual Review of Fluid Mechanics*, *36*, 281–314.
Zeng, Y., & Jansen, M. F. (2021). Ocean circulation on Enceladus with a high-versus low-salinity ocean. *The Planetary Science Journal*, *2*(4), 151. https://doi.org/10.3847/PSJ/ac1114
Zeng, Y., & Jansen, M. F. (2026). Slantwise convection and heat transport in icy moon oceans. *Geophysical Research Letters*, *53*(3), e2025GL118761. https://doi.org/10.1029/2025GL118761
Zhang, Y., Kang, W., & Marshall, J. (2024). Ocean weather systems on icy moons, with application to enceladus. *Science Advances*, *10*(45), eadn6857. https://doi.org/10.1126/sciadv.adn6857
Zhu, P., Manucharyan, G. E., Thompson, A. F., Goodman, J. C., & Vance, S. D. (2017). The influence of meridional ice transport on Europa's ocean stratification and heat content. *Geophysical Research Letters*, *44*(12), 5969–5977. https://doi.org/10.1002/2017GL072996